Catalysis Science & Technology

Accepted Manuscript

ROYAL SOCIETY OF CHEMISTRY

www.rsc.org/catalysis

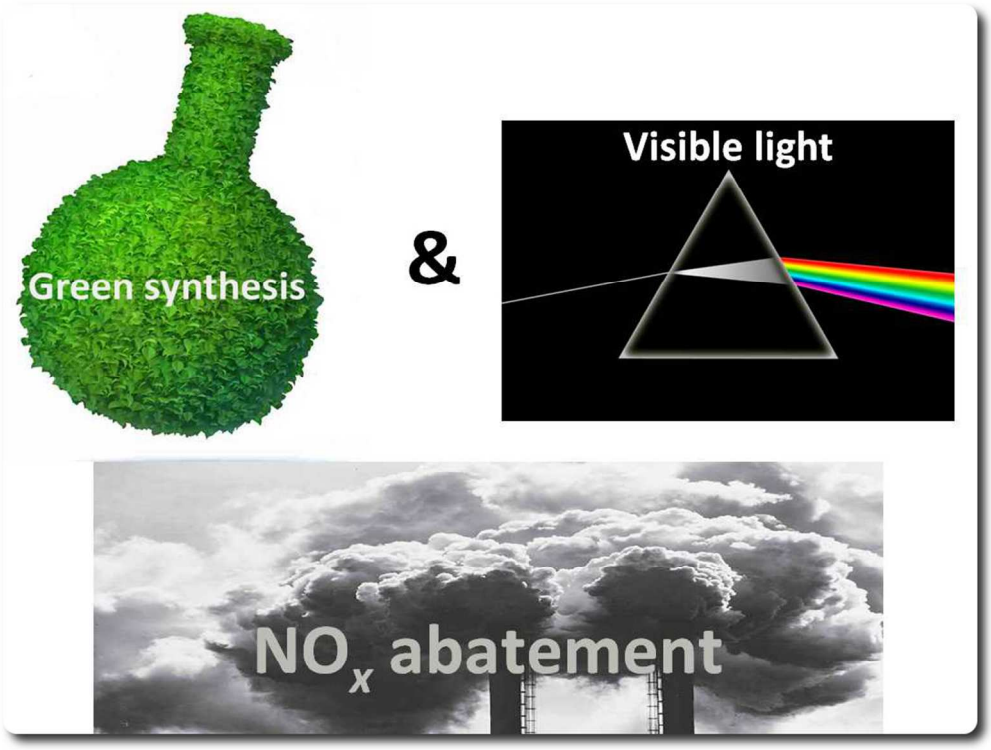

92x70mm (300 x 300 DPI)

Influence of sol counter-ions on the visible light induced photocatalytic behaviour of TiO_2 nanoparticles

D.M. Tobaldi,[a*] R.C. Pullar,[a] R. Binions,[b] A- Belen.-Jorge-Sobrido,[c] P.F. McMillan,[c] M. Saeli,[d] M.P. Seabra,[a] J.A. Labrincha[a]

[a] *Department of Materials and Ceramic Engineering, CICECO, University of Aveiro, Campus Universitário de Santiago, 3810-193 Aveiro, Portugal*

[b] *School of Engineering and Materials Science, Queen Mary University of London, London E1 4NS, United Kingdom*

[c] *Christopher Ingold Building, Department of Chemistry, University College of London, 20 Gordon Street, London, WC1H 0AJ, United Kingdom*

[d] *Dipartimento di Architettura (D'ARCH), Scuola Politecnica, Università degli Studi di Palermo, Viale delle Scienze, 90128, Palermo, Italy*

Abstract

Titanium dioxide (TiO_2) nanoparticles are attracting increasing interest because of their superior photocatalytic and antibacterial properties. Here, aqueous titanium oxy-hydroxide sols were made, using a green synthesis method, from the controlled hydrolysis / peptisation of titanium isopropoxide. Three different mineral acids were used to peptise the sol (HNO_3, HBr and HCl), and provide counter-ions. The influence of nitrate or halide sol counter-ions on size distributions of the starting sols were measured via photon correlation spectroscopy (PCS). Semi-quantitative phase

composition analysis (QPA), on the gels thermally treated at 450 and 600 °C, was determined *via* Rietveld refinement of the X-ray powder diffraction (XRD) patterns. Photocatalytic activity of the prepared samples was also assessed, in gas-solid phase, monitoring NO_x degradation using both solar and white lamps (artificial indoor lightning). Both halides (chlorine or bromine) encouraged the anatase-to-rutile phase transition (ART), resulting in powders containing up to 77 wt% rutile and only 5 wt% brookite after heating to only 450 ºC, with particle sizes ~50 nm, and these produced 100% rutile at 600 ºC. Photocatalytic tests in the gas phase, using a white lamp, showed that the halide-stabilised sols, thermally treated at 450 °C, gave titania with the highest NO_x conversion rate – twice that of Degussa P25.

KEYWORDS: Sol-gel; Sol counter-ions; Titania; Photocatalysis

* Corresponding author. Tel.: +351 234 370 041

E-mail addresses: david.tobaldi@ua.pt; david@davidtobaldi.org

1. Introduction

The application of nanoscale materials could represent a significant scientific contribution to global wellbeing. Nanomaterials are typically structures with dimensions ranging from 1 to 100 nm.[1] They possess unique physiochemical, catalytic, surface and magnetic properties, and these may provide solutions to problems that cannot be dealt with using conventional technologies. Nanotechnologies are already becoming an invaluable tool in the environmental context, *e.g.* for the removal of pollutants from water, air and soil. Nanostructured materials can be incorporated into specific components or devices in the areas of solar energy conversion, catalysis, medicine and environmental remediation, often offering more effective, efficient, durable, environmentally friendly and affordable approaches.[2,3] Compared to those based on conventional bulk materials, this can lead to more cost-effective, and less time- and energy-consuming, solutions, that also generate lower amounts of waste.[4] However, for such widespread use the processing must be economic, and ideally "green" synthesis methods should be essential, with special emphasis on processes that do not require toxic solvents, and will reduce hazardous wastes from the preparation.

Green chemistry, according to Anastas and Warner, is defined as: "the utilisation of a set of principles that reduces or eliminates the use or generation of hazardous substances in the design, manufacture, and application of chemical products".[5] The same authors also defined 12 principles of green chemistry, which are meant as a guide for minimising the use of unsafe products, and maximising the efficiency of chemical processes.[6] Of these 12 principles, the work in this paper directly addresses numbers 3 (less hazardous chemical synthesis), 4 (designing safer chemicals – TiO_2

is non toxic) and 5 (safer solvents and auxiliaries – this method is aqueous based, with no toxic reagents or organic solvents), while also complying with many of the other principles. It can therefore genuinely be called a *Green Chemical* method.

Titanium dioxide (TiO_2) nanoparticles are attracting increasing interest due to their unique physiochemical properties and widespread applications, *i.e.* in photocatalysis, energy materials, antibacterial agents and gas-sensors.[7–14] Of these, photocatalysis is expected to be one of the most important means of challenging many of the emerging problems in modern society, and the potential of heterogeneous photocatalysis with TiO_2 is very wide ranging. Photocatalysis is a particularly promising method of solving problems associated with increasing environmental pollution (both indoor and outdoor, waterborne and airborne), being able to degrade organic and inorganic chemicals in both air and water, and combating global warming and reliance on an oil economy by developing new energy sources (through water splitting to produce hydrogen).[8,15]

In the present work, we report the influence that sol counter-ions have on the photocatalytic activity of TiO_2 nanoparticles. We have previously synthesised TiO_2 nanopowders *via* an aqueous green sol-gel method, using nitrate counter-ions.[16,17] These aqueous titanium oxy-hydroxide sols were made from the controlled peptisation of titanium isopropoxide, hydrolysed using distilled water. Here, three different mineral acids were used to peptise the sol (HNO_3, HBr and HCl), and provide counter-ions. The size distributions of the starting sols were measured via photon correlation spectroscopy (PCS), and average sizes were all found to be between 2-5 nm. The gels were dried in an oven at 75 °C, and then thermally treated at 450 and 600 °C in air. A semi-quantitative phase composition analysis (QPA) of

the calcined samples – and hence an estimate on the influence that counter-ions had on the anatase-to-rutile phase transformation (ART) – was carried out using the Rietveld method on X-ray powder diffraction patterns. Photocatalytic activity of the prepared samples was also assessed – in gas-solid phase, checking NO_x abatement, and in liquid-solid phase monitoring the degradation of an organic dye (methylene blue).

2. Experimental

2.1 Sample Preparation

Aqueous titanium(IV)hydroxide sols were made following the procedure previously reported for nitrate-based sols.[16] This was *via* the controlled hydrolysis of titanium(IV)isopropoxide (Ti-*i*-pr, $Ti(OCH(CH_3)_2)_4$), using distilled water diluted in alcohol which was added dropwise over about 40 min. The water/alcohol solution also contains the peptising acid. One part of Ti-*i*-pr (Aldrich, 97%) was added to four parts of isopropyl alcohol (IPA, propan-2-ol) to make a 20% Ti-*i*-pr solution. This Ti-*i*-pr solution was hydrolysed by the dropwise addition of an excess of water (5:1 water:Ti-*i*-pr) as a 20% solution in IPA. The acid necessary to peptise the sol was also added to this water-IPA solution, in a ratio of Ti^{4+}:acid of 5:1. The acids used were concentrated HNO_3 (Aldrich, 65%), concentrated HCl (VWR AnalaR, 37%) and concentrated HBr (Aldrich, 48%). This water-IPA-acid solution was added dropwise to the Ti-*i*-pr solution at RT, whilst it was mechanically stirred at 800-1200 RPM. The precipitated mixture was evaporated to a white jelly-like mass on a rotary evaporator at 60 ºC and 110-140 mPa. Distilled water was added to restore the mixture to the original volume, then the gelatinous mass was redispersed in a few

min, and the solution evaporated to a jelly like mass again, this time at 60 mPa and 60 ºC. At this stage, when water was added again, the gelatinous mass dispersed to form a sol in 2 min, and the sol was diluted to a concentration of 1 M Ti^{4+}. The process is summarised graphically in Fig. 1. Although the sol particles are nominally titanium hydroxide ($Ti(OH)_4$), from this point on, the sols will be referred to as Ti sols.

All sols were maintained at a 1M concentration, and were shown to be stable for over a week in all cases, and often several weeks. The volume of solvent / water before evaporation on the rotary evaporator was approximately 500 ml in all cases. The as-synthesised gels were dried in an oven at 75 °C, and afterwards the dried gels were heated in a muffle furnace at 450 °C, 600 °C, and 800 °C, under a static air flow. The heating / cooling rate was 5 °C min^{-1}, with a 2 hour dwell time at the selected temperature.

2.2 Sample Characterisation

The size distributions of the starting sols were measured via photon correlation spectroscopy (PCS) – also known as dynamic light scattering (DLS) – using a Zetasizer Nano ZS (Malvern Instruments, UK). 4 drops of the 1M sol were added to a cuvette of water, and measured at room temperature, after being allowed to stabilise for 10 min. The scattering was measured at an angle of 173º, using a 633 nm laser, and assuming the refractive indexes of water and the $Ti(OH)_4$ based sol particles to be 1.33 and 2.50, respectively. Size information was calculated from the correlation function and cumulants analysis using the CONTIN method (an algorithm developed for analysing the autocorrelation function),[18] and number size

values were obtained from refinements using Mie theory, to reflect the true size distribution. Particle sizes were measured between 0.4 and 10,000 nm.

Thermo-gravimetric and differential thermal analyses (TGA/DTA, Setaram Labsys, FR) were performed on the dried gel, in an air flow and with a heating rate of 5 °C min^{-1}, from room temperature (RT) to 900 °C.

A semi-quantitative phase composition analysis (QPA, not accounting for the presence of amorphous phase in the samples) of the calcined titania gels was obtained *via* X-ray diffraction, utilising the Rietveld method. The instrument used was a θ/θ PANalytical X'Pert Pro (NL) diffractometer equipped with a fast RTMS detector (PIXcel 1D, PANalytical, NL), with graphite monochromated Cu Kα radiation (40 kV and 40 mA, 20–115 °2θ range, virtual scan step of 0.0167 °2θ, integration time of 100 s). The Rietveld refinements were accomplished with the GSAS package,[19] and its graphical interface EXPGUI.[20] The starting atomic parameters for anatase, rutile and brookite, described as the space groups $I4_1/amd$, $P4_2/mnm$ and *Pbca* respectively, were taken from a previous work of the present authors.[21] The following parameters were refined: scale-factors, zero-point, 6 coefficients of the shifted Chebyshev function to fit the background, unit cell parameters and profile coefficients – one Gaussian (G_W), an angle-independent term, and two Lorentzian terms, L_X and L_Y, as peak correction for asymmetry.

Diffuse reflectance spectroscopy (DRS) was performed with a Shimadzu UV 3100 (JP) spectrometer, and spectra of the samples were acquired in the UV-Vis range (250-750 nm), with 0.2 nm step-size and using an integrating sphere and a white reference material, both made of $BaSO_4$. The optical band gap (E_g) of the powders was calculated using the differential reflectance method from the obtained

DRS spectra. This method supposes that, plotting the first derivative of reflectance ($dR/d\lambda$) *versus* the wavelength (λ), the maximum value of such a plot corresponds to the E_g of the semiconductor material.[22,23]

With the aim of showing the occurrence of OH groups and/or water adsorbed on the photocatalyst's surface, FT-IR analysis was performed with a Bruker Tensor 27 (DE) spectrometer. The measurements were carried out over the wavenumber range of 4000–300 cm^{-1}, and the powders (2 mg) were mixed with KBr (200 mg, to give 1 wt% of powder in the KBr disks), and pressed into thin pellets. Prior to carrying out the FT-IR analysis, the pellets were stored in an oven at 120 °C for 30 min.

Raman spectra of the samples were acquired in the 50-1000 cm^{-1} wavelength range, with 4 cm^{-1} resolution, on a RFS 100/S (Bruker, DE) equipped with a Nd:YAG laser (1064 nm) as the excitation source.

HR-TEM analysis was assessed on a Jeol JEM 2010 LaB_6 microscope operating at 200 kV; samples were prepared by dispersing the nanoparticles in methanol. And evaporating the suspension drops on carbon-coated copper grids.

The specific surface area (SSA) of the prepared samples was evaluated by the Brunauer–Emmett–Teller method (BET) (Micromeritics Gemini 2380, US) using N_2 as the adsorbate gas.

2.3 Evaluation of Photocatalytic Activity

The photocatalytic activity (PCA) of the prepared samples was assessed both in gas–solid phase and in liquid–solid phase, the former by monitoring the degradation of NO_x, the latter following the degradation of an organic dye (methylene blue, MB) *via* a spectrometer (Shimadzu UV 3100, JP). Evonik Aeroxide (formerly known as

Degussa) P25® photocatalytic powder, hereafter referred to as P25, was used as reference in all the PCA tests.

2.3.1 Gas-solid Phase

The reactor employed for gas-solid phase tests, operating in continuous conditions, as previously described,[17,24] was made of a stainless steel cylinder (35 L in volume); its top was sealed and covered with a glass window, to allow for the light to reach the photocatalyst placed inside it. The light sources employed were a solar lamp (Osram Ultra-Vitalux, 300 W) – re-creating an outdoor situation – and a white light irradiating only in the visible region (Philips LED Bulb Warm white)[25] – hence simulating an artificial indoor lighting. For the solar lamp, the distance between it and the photocatalyst was 85 cm. The light intensity reaching the samples, measured with a radiometer (Delta OHM, HD2302.0, IT), was found to be approximately 3.6 W m^{-2} in the UVA range, and 25 W m^{-2} in the visible-light range. The white lamp was placed 28 cm from the photocatalyst, so as to have a light intensity reaching it of around 7 W m^{-2} in the visible range, and being nil in the UVA.

Samples were prepared in the form of a thin layer of powder, with a constant mass (~0.10 g), and thus approximately constant thickness, in a 6 cm diameter Petri dish. The tests were performed at 27±1 °C (temperature inside the reactor) with a relative humidity of 31%. These parameters – controlled by means of a thermocouple that was placed inside the chamber, and a humidity sensor placed in the inlet pipe – remained stable throughout the tests. The outlet concentration of the pollutant gas was measured using a chemiluminescence analyser (AC-30 M, Environment SA, FR). After having placed the photocatalyst inside the reactor, and covered the glass

window, the inlet gas mixture (prepared using synthetic air and NO_x gas) was allowed to start flowing until it stabilised at a concentration of 0.5 ppmv. Two mass flow controllers were used to prepare such a mixture of air with this concentration of NO_x, and with a flow rate of 1 L min^{-1}. This step was necessary to guarantee the sample saturation, assuring that during the test any measurement of NO_x is solely due to the photocatalytic process (*i.e.* no absorption from the sample, nor from the reactor walls).[26] Once the desired concentration of 0.5 ppmv was attained, the window glass was uncovered, the lamp turned on, and the PCA reaction started. The photocatalytic reaction was deemed to be completed when the pollutant concentration reached a minimum and stable level, and the sample could no longer keep on decomposing any NO_x.

The photocatalytic efficiency was evaluated as the ratio of the removed concentration of NO_x. The conversion rate (%) of the initial NO_x concentration was calculated as:

$$NO_x conversion\% = \frac{(NO_x)_0 - (NO_x)_s}{(NO_x)_0} \times 100 \quad (1)$$

where $(NO_x)_0$ and $(NO_x)_S$ are, respectively, the initial NO_x and the NO_x concentration (both expressed as ppmv) after a certain irradiation time.[27] Moreover, with the aim of having a better comparison between the tested samples, data relative to the first 20 min of reaction time were elaborated according to a first order kinetic law.

2.3.2 Liquid-solid Phase

The liquid–solid phase tests were performed at RT in a cylindrical photocatalytic reactor (Pyrex) containing a water solution of the dye (0.5 L), whose initial concentration was 5 mg L^{-1}.[16] The concentration of the photocatalyst in the slurry was 0.25 g L^{-1}. In order to mix the solution thoroughly, the slurry was stirred throughout the reaction and the reactor was covered with a watch-glass, so as to avoid the evaporation of the solution. The lightning of the reacting system was ensured by placing two lamps at the side of the reactor – the distance between the lamps and the reactor was 5 cm. The UVA-light source was a germicidal lamp (Philips PL-S 9 W, NL), having an irradiance – measured with a radiometer (Delta OHM, HD2302.0, IT) – of approximately 13 W m^{-2} in the UVA range, while the visible-light source was a fluorescent lamp (Philips master PL-S 2 P 9 W/840, NL), with an irradiance of about 50 W m^{-2} in the visible region and 0.6 W m^{-2} in the UVA region (hence considered negligible). In the experiments, the photocatalytic degradation of MB was monitored by sampling from the reactor, at regular time intervals, 4 mL of the slurry. The powders in the samples were separated by centrifugation, and then the MB concentration in the liquid was determined by measuring the absorbance in a spectrophotometer at a wavelength of 665 nm. The extent of MB photocatalytic degradation ξ, was evaluated as:

$$\xi\% = \frac{C_0 - C_S}{C_0} \times 100 \qquad (2)$$

where C_0 is the initial MB concentration and C_S is the concentration after a certain UVA/visible irradiation time. Control experiments to determine if a likely photolysis of the MB dye affected the tests, under direct UVA and visible-light irradiation, were performed prior to testing the photocatalytic activity of the prepared samples.

The photocatalytic reaction being a pseudo first-order reaction, its apparent first-order constant (k'_{app}) can be evaluated as:

$$\ln\left(\frac{C_0}{C}\right) = k'_{app}\, t \qquad (3)$$

where C_0 is the initial concentration of MB and C is its concentration after a certain irradiation time t. Therefore, the plot of $\ln(C_0/C)$ *versus* the irradiation time t, gives a straight line, whose slope corresponds to the value of the pseudo first-order apparent rate constant (k'_{app}).[28]

The total irradiation time was set at 7 h, and the lights (UVA or visible) were turned on 30 min after having put the photocatalyst in the reacting system, in order to allow adsorption/desorption of the dye onto the powders to occur and stabilise.

Furthermore, as dyes can be excited by visible-light irradiation, they can act as a sensitiser, with electron injection from the photo-excited dye to the photocatalyst.[29,30] This implies that such an electron transfer may destroy the regular distribution of conjugated bonds within the dye molecule, and this may cause its decolourisation, but not its mineralisation.[31] Furthermore, MB is reported to undergo to a reduced, colourless form, known as leuco-methylene blue (LMB).[32] Therefore, aiming at verifying if, under visible-light irradiation, there was a ‘‘real’’ photocatalytic reaction, or on the contrary, a (total or partial) decolouration of the dye by photo-sensitising effects, total organic carbon (TOC) determination was performed, via a TOC-meter (TOC 1200, Thermo Electron Corporation, US).

3. Results and Discussion

3.1 Sol preparation and characterisation

The process used to make the HNO_3 peptised sols was identical to that reported by the authors previously, to make pure and W and Ag doped titania nanoparticles.[16] The Ti-*i*-pr solution was hydrolysed by the dropwise addition of a water-IPA-HNO_3 solution, and at the end of the addition a milky white mixture with a slightly yellowish tinge resulted. The solvent was removed under vacuum on a rotary evaporator at 140 mbar, and was dried to a white jelly-like mass, with a slight yellowish tinge. This gelatinous mass was redispersed in water and dried to a jelly-like mass again, this time with a white colour and a slight bluish tinge. When water was added again, this gelatinous mass rapidly dispersed to form a sol in 2 min, with a slightly bluish tinge. Fig. 2 shows the number average sol particle size distribution from PCS measurements, measured 3 days after the sols were produced. All particles in the HNO_3 sol were between 2-10 nm, with 98% between 2-6 nm, and 80% between 2.33-4.85 nm. The mean was 3.61 nm with a standard deviation of 1.23 nm.

To make the HCl-peptised sol, the Ti-*i*-pr solution was hydrolysed by the dropwise addition of a water-IPA-HCl solution. After the addition a viscous white, thixotropic jelly had formed, which needed continuous stirring at 1200 RPM to break it up, unlike the smoother suspension-like end product obtained with HNO_3. In previous work on aqueous sol-gel derived YAG ($Y_3Al_5O_{12}$) and ferrites ($Fe(OH)_3$ sols) by Pullar *et al.*, it has been reported that chloride based sols became much more gelatinous and thixotropic, with much more evidence of linking between the sol particles.[33,34] These chloride based sols were also less stable than their nitrate counterparts, and flocculated/precipitated at lower concentrations.[35] Increased

bonding between the chloride stabilised sol particles was also observed when fibres were blow spun from these, and the persistent presence of chloride in the material up to 1000 ºC delayed the formation of YAG and complex hexaferrite phases.[36,37]

The solvent was evaporated at 120 mbar, although it was more difficult to remove the alcohol, indicating a greater degree of bonding in the water/alcohol/chlorine mixture, resulting in a bulky white gelatinous solid. This was redispersed in water, and evaporated to a fine, viscous gel, which slowly dispersed to give a sol when more water was added. The sol was a yellowish, off-white colour, not bluish as with the nitrate counter-ions, indicating a different particle size. This was seen in the PCS measurements (Fig. 2), as the size range was smaller in the HCl based sol, between 1.5-5.6 nm, with 99% between 1.5-3.6 nm, and 78.5% between 1.50-2.32 nm. The mean was 2.20 nm with a standard deviation of 0.57 nm. Therefore, despite the increased level of interparticle structure, the HCl peptised sol has a smaller average particle size and upper limit of size. In this work, the Ti sol with Cl^- counter-ions has a number average diameter approximately 60% of that with NO_3^-. In previous work by Pullar *et al.* on ferrite sols, there was a similar difference between Fe_2O_3 sols with different counter-ions, with a HCl-peptised $Fe(OH)_{3-2x}O_x$ sol also having a slightly smaller number average (5.1 *vs.* 6.4 nm) and upper limit than a NO_3^- sol.[35]

The HBr peptised sol was made by the dropwise addition of a water-IPA-HBr solution, forming a more gelatinous, but less thixotropic, precipitate than that observed with HCl. A lower pressure of 110 mbar was required to remove the IPA, to give a white gelatinous phase. This was redispersed in water, and then evaporated to a yellow, glassy gel. When more water was added, the gel instantly dispersed within 30 seconds to give a darker, slightly-orange coloured, more transparent sol.

This was reflected in the PCS measurements (Fig. 2), as the size range was the largest of all in the HBr based sol, between 3-12 nm, with 99% between 3.1-7.5 nm, and 84.5% between 3.61-5.61 nm. The mean was 4.55 nm with a standard deviation of 1.11 nm.

3.2 Thermal Behaviour

The TGA/DTA results are depicted in Fig. 3a-c. In the TGA plot of the titania sol made with HNO_3 (Fig. S1a, Electronic Supplementary Information), there were two weight-loss regions: the first one had a mid-point at about 125 °C, corresponding to the loss of water from the porous gel network, and this region accounted for half of the total weight-loss. The major second thermal event was centred around 250 °C, representing the decomposition of nitrates and any remaining organic compounds in the gel.[38] Beyond ~400 °C, there was no further significant weight-loss, as indicated by the plateau in the TGA plot; the total weight-loss of the material was about 28%. As can be seen from DTA analysis, the prominent endothermic event at approximately 125 °C, and the exothermic event at about 250 °C, indicated the processes discussed above for the TGA analysis, while the broad exothermic peak, with a maximum at around 485 °C should represent the ongoing ART.[16]

However, the samples made with Cl^- and Br^- had subtly different TGA/DTA plots (Fig. S2b,c). With halides present, the loss of water from the porous gel network initiated at a lower temperature, about 95 °C, but instead of showing a single large endothermic event, the DTA plot exhibited two clear, smaller endothermic peaks, one at 90 °C, and a broader exotherm around 130-145 °C. This suggested that there is a two-step loss of water with the halides. These regions also showed a greater

weight-loss for the halides during the loss-of-water phase (compared to ~15% for NO_3^- at 150 ºC), suggesting that the dried gel had a higher water content when made from halides. The HCl sample had a second dehydration endotherm around 130 ºC, and this process had completed by around 150 ºC with a weight loss of 19%. The HBr sample exhibited a much broader second endotherm centred around 145 ºC, but the process continued until 200 ºC, with a weight loss of 22% at this temperature.

After this dehydration process, the HCl sample exhibited a sharp exotherm around 200 ºC, and a steady, but diminishing, weight loss with increasing temperature up to around 400 ºC, at which point it had lost 32% weight. This represents the combustion of any remaining organic species, and the partial loss of chlorine. However, there remains a small but significant continuous weight loss up to 900 ºC, with a final loss of 34% at this temperature (Fig. S1b). This agrees with the findings of Pullar *et al.* in their work on similar aqueous, chloride-peptised iron (III) hydroxide-based sols, in which most of the chlorine was lost at 200 ºC, but the material still contained around 5 wt% chlorine up to 600 ºC, with 2.5 wt% remaining at 800 ºC and a temperature of 1000 ºC being required to remove all of the highly persistent chlorine.[36]

Pullar *et al.* also found that, at 200 ºC, 22 wt% bromine was retained in HBr peptised aqueous iron (III) hydroxide-based gels. However, by 400 ºC this had fallen to ~6 wt% bromine, under 5 wt% at 600 ºC and all bromine was removed by 800 ºC.[36] This supports the results seen here with the HBr sample, which exhibited a very broad exotherm centred around 250 ºC, and with a greater rate of weight loss, up to 34% at 365 ºC, than the HCl sample (Fig. S1c). This weight loss continued until 600 ºC, by which point 37% had been lost, and no significant loss occurred with further temperature increase. This suggests that, as seen in the iron (III) hydroxide gels,

bromine required a greater initial temperature to begin its removal, but it was less persistent than chlorine, and completed the process at a temperature of 600 ºC in these titania sols.

No separate peak was seen for the ART in the HCl or HBr samples, suggesting that it is a steady, continuous process that may initiate at the onset of halide loss from the systems.

3.3 X-ray Analysis

XRD patterns of the samples are shown in Fig. 3. The semi-QPA of the thermally treated gels, by means of XRD, is shown in Table 1; an example of a Rietveld graphical output (sample HNO_3 450), is depicted in Fig. S2. It should be noted that this evaluation was made without taking into account the presence of any amorphous phase in the samples, hence only accounting for the crystalline phases that are in the samples.

As depicted in the HR-TEM micrographs (Fig. 4a,b), the thermally treated nanopowders are all composed of strongly aggregated, and irregularly shaped, nanoparticles. Also, the size distribution seems to be wide, varying between 10–40 nm.

The reference commercial photocatalyst P25 is a mixture of anatase, rutile and amorphous phase (76.3 wt%, 10.6 wt%, and 13.0 wt%, respectively).[39] For the titania gels thermally treated at 450 °C (Fig. 3a), it was seen that using nitrate counter-ions led to a strong presence of crystalline anatase (34.6 wt%), together with rutile (50.7 wt%) and also a significant amount of brookite (14.6 wt%). On the other hand, the presence of chloride and bromide counter-ions accelerated the brookite-to-rutile

phase transformation: in these samples heated to 450 °C, there is only very small amount of brookite (3.4 wt% with HCl, 5.3 wt% with HBr). That accelerating behaviour has been attributed to the adsorbed halides, which are not easily removed from the surface of titania even by heating at relatively at high temperature,[40] as also seen in the *thermal behaviour* section. Hence, halides will form oxygen vacancies on the surface, thus enhancing the ART.[41] The presence of brookite would otherwise be expected, as the pH of the starting sols is highly acidic (pH ~1), and this favours brookite crystallisation.[21,42] Moreover, the sample made with Cl^- as counter-ions and thermally treated at 450 °C was composed of 19.4 wt% anatase and 77.2 wt% rutile, making it the sample with the smallest amount of anatase. By contrast, the sol made with Br^- as counter-ions, thermally treated at 450 °C, had 27.4 wt% anatase and 67.3 wt% rutile. Hence, from these results, the following trend can be inferred in terms of counter-ions delaying the ART mechanism (which is a nucleation and growth mechanism):[43] NO_3^- >Br^- >Cl^-. This is shown in Fig.S3.

To further support this, at the temperature of 600 °C (Fig. 3b), the HNO_3 sample was the only one still containing even a small amount of anatase (1.8 wt%), the other two samples having completely accomplished the ART, and hence being composed only of rutile as a crystalline phase. At the temperature of 800 °C, every sample has fully accomplished the ART (Fig. 3c).

3.4 Raman, Optical and FT-IR Spectroscopy

Raman spectra of the samples are depicted in Figure 5, and the anatase, rutile and brookite Raman modes are shown in Table S1. Although this technique cannot be used for quantitative investigation,[44] Raman analysis showed the presence of anatase,

rutile and brookite in samples thermally treated at 450 °C (Fig. 5a), consistent with the XRD data. At 600 °C, the only sample showing the presence of some residual anatase was that made with HNO_3, the ART being completed in the halide samples (Fig. 5b). At 800 °C, consistent with XRD, Raman spectra showed only the presence of rutile in all the samples (Fig. 5c). In these samples, a broad band was also present, centred around 250 cm^{-1}. This is a characteristic feature of rutile,[45] and its complex nature has been attributed to either second-order scattering,[46] or disorder effects.[47]

Optical spectroscopy was used with the aim of investigating the (optical) E_g of the samples. DRS spectra are shown in Figure 6a,b, while the optical E_g of the samples are listed in Table 2. All the samples, thermally treated at both temperatures, had a single absorption band below approximately 410 nm, which was ascribed to the metal–ligand charge transfer (MLCT) in titania.[48] Moreover, samples with Cl^- and Br^- as CI in the starting sols, and thermally treated at the two maximum temperatures, show also to absorb in the visible region of the spectrum (410-550 nm; 3.02-2.25 eV), as depicted in the inset of Fig. 6a. Though this is not a direct evidence of Cl^- and Br^- incorporation into TiO_2, these absorptions might be attributed to *F*-centres, that are associated with oxygen vacancies, as suggested by Kuznetsov and Serpone.[49] By analogy with other literature data, we suggest that such absorptions might be the result of a mid-gap band (M_g) being accommodated within the TiO_2 E_g,[50,51] without modifying it. The E_g of the samples was calculated by the differential reflectance method, and the resulting curves were effectively fitted with a Gaussian function, the maximum values being found from that fitting. The E_gs were all attributed to rutile (Table 2 and Fig. 6c), being consistent with its expected E_g value of 3.02 eV (411 nm).[52] It should be noted that with the method employed in the present investigation,

the curve of anatase might overlap that of rutile, hence the E_g of rutile may "hide" that of anatase

FT-IR spectra of the samples thermally treated at 450 °C are depicted in Figure 7. The band in the range of 400-600 cm^{-1}, observed in all the FT-IR spectra, belongs to the Ti–O–Ti vibrations. The peak at ~1620 cm^{-1} corresponds to the bending vibrations of O–H, while the broad band at approximately 3430 cm^{-1} is attributed to the surface-adsorbed hydroxyl groups.[53] From a comparison amongst the tested samples, it can be seen that there was no marked difference between them, with the sol made with NO_3^- as counter-ions, and calcined at 450 °C, having slightly more surface hydroxyl groups on its surface. These, being able to accept the photogenerated holes, can create hydroxyl radicals, hence oxidising molecules adsorbed on the photocatalyst surface.[54]

4.1 Photocatalytic Activity

4.1.1 Gas-solid Phase

The NO_x abatement results are shown in Figure 8a,b and Table 3. When using a lamp with a significant UV component, the best performing photocatalyst is the reference commercial sample of P25. The PCA of the prepared samples followed the trend: $Br^- > NO_3^- > Cl^-$. The same degradation trend is shown in the initial (first 20 min of reaction) pseudo-first order kinetic constants (Table 3). A possible explanation of the higher activity in gas-solid phase of the HBr sample can be given by (residual) bromide species that remain in the catalyst structure (as qualitatively shown by TGA/DTA analyses): it has been stated that even small amounts of these species are able to cause substantial improvement in the catalytic properties of

oxides.[55,56] These results are also consistent with those reported by Luo et al.,[57] who showed that Cl^- modified TiO_2 had a lower activity than both P25 and Br^- modified TiO_2 under UV-light irradiation; these authors attributed that to a narrowing of the TiO_2 band gap, due to Br^-.

Furthermore, as can be seen in Fig. 8a,b, after 45 minutes of irradiation time, following an initial degradation, the pollutant concentration reached a plateau, and the samples could no longer keep on decomposing NO_x. This deactivating behaviour of TiO_2 is caused by the oxidation of NO_2 to HNO_3. The O^{2-} and OH• radicals formed during photocatalysis react with the pollutant gas, producing NO_2 and HNO_3:[58]

$$NO + OH\bullet \rightarrow NO_2 + H^+ \quad (4)$$

$$NO + O^{2-} \rightarrow NO_3^- \quad (5)$$

$$NO_2 + OH\bullet \rightarrow NO_3^- + H^+ \rightarrow HNO_3 \quad (6)$$

Thus, the reaction path for NO_x conversion is mediated by OH• radicals. Furthermore, as been reported by Ohko *et al*., the HNO_3 produced on the surface of TiO_2 acts as a physical barrier, inhibiting the photocatalytic reaction.[59] Samples fired at 600 °C all had a lower photocatalytic activity (*cf* Table 3), with sample HBr being inactive. In general, this behaviour is most likely due to the completion of the ART (except for the HNO_3 sample, that still contained 1.8wt% anatase), and a lowering of the SSA as a consequence of a coarsening of the titania particles. Interestingly, the only sample maintaining a comparable activity with its counterpart thermally treated at 450 °C is sample HCl 600. At 800 °C, no sample was shown to be photocatalytically active (data not shown in Table 3).

Results for the photocatalytic tests with the white lamp are shown in Fig. 8b and Table 3. Under white-light exposure, HNO_3 and P25 had virtually the same low degree of activity (18.9% and 19.8%, respectively). On the contrary, HCl and HBr samples had much greater activities (36.1% and 34.2%, respectively) when using a light source irradiating only in the visible region of the solar spectrum. This was also confirmed by the pseudo-first order kinetic constants of the initial first 20 min of reaction, as shown in Table 3: halide-stabilised sols had a PCA twice higher than P25. This might be due to the concomitant presence of nano-anatase and rutile,[60,61] and also to the higher amount of rutile in these samples. In fact, it has been reported that, when nanostructured, rutile can be a visible-light active photocatalyst.[62] It has been shown by Hurum *et al.*,[63] that the visible-light response of P25 – a mixture of anatase, rutile and amorphous phase [39] – is actually due to the presence of small rutile crystallites amongst those of anatase. They claimed that the points of contact between these anatase and rutile crystals allow for rapid electron transfer from rutile to anatase, and hence, rutile acts as an ''antenna'', able to extend the PCA into visible wavelengths. As a matter of fact, all of these samples had calculated E_g values in the visible-light region (Table 2). Additionally, it has also been stated that the presence of residual Br^- and Cl^-, as shown by TG/DTA and also by DRS analyses, can lead to them replacing oxygen in the titania lattice (indirectly proven by the accelerating behaviour of the ART by the halides), thus causing absorption in the visible light range, and enhancing photocatalytic activity under visible light irradiation.[57] The increase of the firing temperature to 600 and 800 °C led to a loss of photocatalytic activity in all the samples, due to the aforementioned reasons.

4.1.2 Liquid-solid Phase

Liquid-solid and gas-solid phase results cannot be directly compared, as they employed two different reactors, a different initial concentration of target pollutant and photocatalyst, and different lamps with different irradiances (both in the UVA and visible-light region). Notwithstanding, all the samples were also shown to be photocatalytically active in the liquid-solid phase regime. For the liquid-solid phase tests, the influence of photolysis on the photocatalytic experiments in liquid-solid phase was found to be negligible, its values being equal to 3%, and 1%, under UVA and visible-light irradiation, respectively (these data are not reported in Figure 9). All samples thermally treated at 450 °C had virtually identical photocatalytic efficiency under UVA irradiation (Fig. 9a) – but greatly lower than the reference P25, in which MB degradation was accomplished in two hours irradiation time – degrading almost all the organic dye, the photocatalytic efficiency values (ξ%) being equal to 98%, 93% and 95% for the HNO_3, HCl and HBr samples, respectively. In this case, even though the HNO_3 sample thermally treated at 450 °C had a higher SSA than the halide-stabilised samples (Table 2), this did not dramatically affected its PCA, and neither did its higher anatase content (Fig. S3). The increase of the thermal treatment temperature to 600 °C caused a general decrease of the photocatalytic activity under UVA light irradiation (Fig. 9b). The sample with Cl^- as counter-ions in the sol was the best photocatalyst, degrading 75% of the original dye; the least efficient sample was that with Br^- as counter-ions in the sol, having ξ% equal to only 39%. This decrease in the PCA was not only due to a lowering of the SSA (which usually accompanies a growth in particle size), but also due to the completion of the ART, which was only partial in the case of the HNO_3 sample.

All the samples were shown to possess PCA under visible-light exposure, even if to a lesser extent compared to UVA exposure (Fig. 9c,d). The HCl and HBr samples thermally treated at 450 °C, which contained more rutile, were more active photocatalysts under visible-light exposure (ξ% = 78% and 76%, respectively). The HNO_3 sample was the least active one, but still with a photocatalytic efficiency value of 59%. However, under visible-light exposure, every sample had a photocatalytic efficiency higher than the reference P25 sample. Furthermore, in liquid-solid phase and under visible-light irradiation, the HCl and HBr samples were shown to possess higher PCAs, with regard to both the HNO_3 and P25reference samples. These results are in strong agreement with those obtained in gas-solid phase, and hence attributable to the presence of residual Br^- and Cl^-, as has been previously stated.[57]

TOC results (with the HNO_3 sample thermally treated at 450 °C, and P25) showed that under visible-light exposure, there was an actual decrease in the organic carbon content (*i.e.* there was a decrease in the normalised organic carbon content: the value measured at the end of the reaction was 22.5% and 74.1% for HNO_3 and P25 samples, respectively). Hence, by analogy, we believe that the other tested samples also possessed this activity. In any case, with the available data, it has to be underlined that potential dye-sensitising effects (decolourisation) – together with a "real" photocatalytic reaction (mineralisation of the target pollutant) – cannot be excluded *a priori*.[64]

4. Conclusions

Nanopowders of titania were made by a green nanosynthesis technique based upon environmentally-benign aqueous sol-gel techniques. The effects of having

NO_3^-, Cl^- or Br^- counter ions on the sol properties and the resulting nanopowders were investigated. The halides encouraged the anatase-to-rutile transition (ART) phase, resulting in powders with up to 77 wt% rutile and only 5 wt% brookite after heating to only 450 ºC, and they produced 100% rutile after 600 ºC. They also had fine particle sizes, estimated to be ~50 nm after 450 ºC, while the nitrate-stabilised sol gave 98% rutile with an estimated size of 92 nm after heating to 600 ºC. In the gas phase photocatalytic tests, using a solar lamp, the bromide-stabilised sol gave titania with the highest NO_x conversion rate of >30% after 30 mins. Notwithstanding, when using a light source irradiating only in the visible region of the solar spectrum (white lamp) – aimed at re-creating artificial indoor lightning – halide-stabilised sols (thermally treated at 450 °C) had a PCA twice as high as those of the HNO_3 sample and the P25commercial reference sample.

Acknowledgements

D.M. Tobaldi is grateful to the ECO-SEE project (European Union's Seventh Framework Programme funding, grant agreement no 609234). Authors acknowledge PEst-C/CTM/LA0011/2013 programme. M.P. Seabra and R.C. Pullar wish to thank the FCT Ciência2008 programme for supporting this work.

References

1. G. Schmid, *Nanoparticles: From Theory to Application*, John Wiley & Sons, 2011.
2. T. Masciangioli and W.-X. Zhang, *Environ. Sci. Technol.*, 2003, **37**, 102A–108A.
3. M. A. Albrecht, C. W. Evans, and C. L. Raston, *Green Chem.*, 2006, **8**, 417–432.
4. J. E. Hutchison, *ACS Nano*, 2008, **2**, 395–402.

5. P. T. Anastas and J. Warner, *Green chemistry: theory and practice*, Oxford University Press, Oxford [England]; New York, 1998.
6. <"The Twelve Principles of Green Chemistry" http://www.acs.org/content/acs/en/greenchemistry/what-is-greenchemistry/principles/12-principles-of-green-chemistry.html> (Accessed April 2014).
7. A. Fujishima and K. Honda, *Nature*, 1972, **238**, 37–38.
8. A. Fujishima, T. N. Rao, and D. A. Tryk, *J. Photochem. Photobiol. C Photochem. Rev.*, 2000, **1**, 1–21.
9. B. O'Regan and M. Grätzel, *Nature*, 1991, **353**, 737–740.
10. M. Grätzel, *J. Photochem. Photobiol. C Photochem. Rev.*, 2003, **4**, 145–153.
11. L. Kavan, *J. Electrochem. Soc.*, 1996, **143**, 394.
12. K. Sunada, Y. Kikuchi, K. Hashimoto, and A. Fujishima, *Environ. Sci. Technol.*, 1998, **32**, 726–728.
13. M. R. Hoffmann, S. T. Martin, W. Choi, and D. W. Bahnemann, *Chem. Rev.*, 1995, **95**, 69–96.
14. D. Chen and R. A. Caruso, *Adv. Funct. Mater.*, 2013, **23**, 1356–1374.
15. J.-M. Herrmann, C. Duchamp, M. Karkmaz, B. T. Hoai, H. Lachheb, E. Puzenat, and C. Guillard, *J. Hazard. Mater.*, 2007, **146**, 624–629.
16. D. M. Tobaldi, R. C. Pullar, A. F. Gualtieri, M. P. Seabra, and J. A. Labrincha, *Chem. Eng. J.*, 2013, **214**, 364–375.
17. D. M. Tobaldi, C. Piccirillo, R. C. Pullar, A. F. Gualtieri, M. P. Seabra, P. M. L. Castro, and J. A. Labrincha, *J. Phys. Chem. C*, 2014, **118**, 4751–4766.
18. S. W. Provencher, *Comput. Phys. Commun.*, 1982, **27**, 229–242.

19. A. C. Larson and R. B. Von Dreele, *General Structure Analysis System (GSAS)*, Los Alamos National Laboratory Report LAUR, 2004.

20. B. H. Toby, *J. Appl. Crystallogr.*, 2001, **34**, 210–213.

21. D. M. Tobaldi, R. C. Pullar, A. F. Gualtieri, M. P. Seabra, and J. A. Labrincha, *Acta Mater.*, 2013, **61**, 5571–5585.

22. S. Komornicki, M. Radecka, and P. Sobaś, *Mater. Res. Bull.*, 2004, **39**, 2007–2017.

23. D. M. Tobaldi, L. Gao, A. F. Gualtieri, A. Sever Škapin, A. Tucci, and C. Giacobbe, *J. Am. Ceram. Soc.*, 2012, **95**, 1709–1716.

24. S. S. Lucas, V. M. Ferreira, and J. L. B. de Aguiar, *Cem. Concr. Res.*, 2013, **43**, 112–120.

25.<http://download.p4c.philips.com/files/8/8718291193029/8718291193029_spd_itait.pdf> (accessed April 2014).

26. U. I. Gaya and A. H. Abdullah, *J. Photochem. Photobiol. C Photochem. Rev.*, 2008, **9**, 1–12.

27. F. L. Toma, G. Bertrand, D. Klein, and C. Coddet, *Environ. Chem. Lett.*, 2004, **2**, 117–121.

28. H. Al-Ekabi and N. Serpone, *J. Phys. Chem.*, 1988, **92**, 5726–5731.

29. M. Vautier, C. Guillard, and J.-M. Herrmann, *J. Catal.*, 2001, **201**, 46–59.

30. X. Yan, T. Ohno, K. Nishijima, R. Abe, and B. Ohtani, *Chem. Phys. Lett.*, 2006, **429**, 606–610.

31. J.-M. Herrmann, *Appl. Catal. B Environ.*, 2010, **99**, 461–468.

32. C. Yogi, K. Kojima, T. Takai, and N. Wada, *J. Mater. Sci.*, 2009, **44**, 821–827.

33. R. C. Pullar, M. D. Taylor, and A. K. Bhattacharya, *J. Mater. Res.*, 2001, **16**, 3162–3169.

34. R. C. Pullar and A. K. Bhattacharya, *Mater. Lett.*, 1999, **39**, 173–178.

35. R. C. Pullar, M. D. Taylor, and A. K. Bhattacharya, *J. Eur. Ceram. Soc.*, 2002, **22**, 2039–2045.

36. R. C. Pullar, M. H. Stacey, M. D. Taylor, and A. K. Bhattacharya, *Acta Mater.*, 2001, **49**, 4241–4250.

37. R. C. Pullar, M. D. Taylor, and A. K. Bhattacharya, *J. Eur. Ceram. Soc.*, 1999, **19**, 1747–1758.

38. K.-N. P. Kumar, K. Keizer, and A. J. Burggraaf, *J. Mater. Chem.*, 1993, **3**, 1141–1149.

39. D. M. Tobaldi, R. C. Pullar, M. P. Seabra, and J. A. Labrincha, *Mater. Lett.*, 2014, **122**, 345–347.

40. P. Jackson and G. D. Parfitt, *Trans. Faraday Soc.*, 1971, **67**, 2469.

41. J. A. Gamboa and D. M. Pasquevich, *J. Am. Ceram. Soc.*, 1992, **75**, 2934–2938.

42. A. Pottier, C. Chanéac, E. Tronc, L. Mazerolles, and J.-P. Jolivet, *J. Mater. Chem.*, 2001, **11**, 1116–1121.

43. R. D. Shannon and J. A. Pask, *J. Am. Ceram. Soc.*, 1965, **48**, 391–398.

44. C. Piccirillo, C. W. Dunnill, R. C. Pullar, D. M. Tobaldi, J. A. Labrincha, I. P. Parkin, M. M. Pintado, and P. M. L. Castro, *J. Mater. Chem. A*, 2013, **1**, 6452–6461.

45. D. M. Tobaldi, R. C. Pullar, A. S. Škapin, M. P. Seabra, and J. A. Labrincha, *Mater. Res. Bull.*, 2014, **50**, 183–190.

46. M. Gotić, M. Ivanda, S. Popović, S. Musić, A. Sekulić, A. Turković, and K. Furić, *J. Raman Spectrosc.*, 1997, **28**, 555–558.

47. O. Frank, M. Zukalova, B. Laskova, J. Kürti, J. Koltai, and L. Kavan, *Phys. Chem. Chem. Phys.*, 2012, **14**, 14567.

48. F. C. Hawthorne and Mineralogical Society of America, Mineralogical Society of America, 1988.

49. V. N. Kuznetsov and N. Serpone, *J. Phys. Chem. C*, 2009, **113**, 15110–15123.

50. M. Bellardita, M. Addamo, A. D. Paola, L. Palmisano, and A. M. Venezia, *Phys. Chem. Chem. Phys.*, 2009, **11**, 4084–4093.

51. F. Spadavecchia, G. Cappelletti, S. Ardizzone, C. L. Bianchi, S. Cappelli, C. Oliva, P. Scardi, M. Leoni, and P. Fermo, *Appl. Catal. B Environ.*, 2010, **96**, 314–322.

52. S.-D. Mo and W. Y. Ching, *Phys. Rev. B*, 1995, **51**, 13023–13032.

53. D. M. Tobaldi, A. Tucci, G. Camera-Roda, G. Baldi, and L. Esposito, *J. Eur. Ceram. Soc.*, 2008, **28**, 2645–2652.

54. G. Balasubramanian, D. Dionysiou, M. Suidan, I. Baudin, and J. Laine, *Appl. Catal. B Environ.*, 2004, **47**, 73–84.

55. B. Li and H. Metiu, *J. Phys. Chem. C*, 2012, **116**, 4137–4148.

56. S. Chrétien and H. Metiu, *J. Chem. Phys.*, 2008, **128**, 044714.

57. H. Luo, T. Takata, Y. Lee, J. Zhao, K. Domen, and Yan, *Chem. Mater.*, 2004, **16**, 846–849.

58. J. Lasek, Y.-H. Yu, and J. C. S. Wu, *J. Photochem. Photobiol. C Photochem. Rev.*, 2013, **14**, 29–52.

59. Y. Ohko, Y. Nakamura, A. Fukuda, S. Matsuzawa, and K. Takeuchi, *J. Phys. Chem. C*, 2008, **112**, 10502–10508.

60. Z. Ding, G. Q. Lu, and P. F. Greenfield, *J. Phys. Chem. B*, 2000, **104**, 4815–4820.

61. T. Ohno, K. Tokieda, S. Higashida, and M. Matsumura, *Appl. Catal. Gen.*, 2003, **244**, 383–391.

62. S. Yin, H. Hasegawa, D. Maeda, M. Ishitsuka, and T. Sato, *J. Photochem. Photobiol. Chem.*, 2004, **163**, 1–8.

63. D. C. Hurum, A. G. Agrios, K. A. Gray, T. Rajh, and M. C. Thurnauer, *J. Phys. Chem. B*, 2003, **107**, 4545–4549.

64. M. Stylidi, *Appl. Catal. B Environ.*, 2004, **47**, 189–201.

65. G. A. Tompsett, G. A. Bowmaker, R. P. Cooney, J. B. Metson, K. A. Rodgers, and J. M. Seakins, *J. Raman Spectrosc.*, 1995, **26**, 57–62.

66. D. Bersani, P. P. Lottici, and X.-Z. Ding, *Appl. Phys. Lett.*, 1998, **72**, 73.

67. A. Mattsson and L. Österlund, *J. Phys. Chem. C*, 2010, **114**, 14121–14132.

TABLES

Table 1 – Semi-quantitative phase composition of the thermally treated titania gels, as obtained *via* Rietveld refinements.

Sample	No. of variables	Agreement factors			Phase composition		
		R^2_F (%)	R_{wp} (%)	χ^2	anatase (wt%)	rutile (wt%)	brookite (wt%)
HNO_3 450	24	4.10	6.59	1.57	34.6(2)	50.7(1)	14.6(4)
HCl 450	23	5.81	4.33	3.75	19.4(2)	77.2(1)	3.4(3)
HBr 450	22	4.47	4.02	3.64	27.4(1)	67.3(1)	5.3(4)
HNO_3 600	19	3.14	8.28	1.78	1.8(1)	98.2(1)	–
HCl 600	14	5.69	4.95	5.34	–	100	–
HBr 600	15	5.44	5.12	5.21	–	100	–

Table 2 – Optical energy band-gap (E_g) and specific surface area (SSA) of the dried and thermally treated gels. Diameter in nm estimated from $D = 6000 / (SSA * \rho)$, where $\rho = 4.2$ g cm^{-3} (rutile).

	Optical E_g (eV)			
Sample	anatase	rutile	SSA_{BET} (m^2 g^{-1})	D, estimated diameter (nm)
HNO_3 450	–	3.06±0.01	41.9	34
HCl 450	–	3.05±0.01	28.4	50
HBr 450	–	3.04±0.01	25.7	56
HNO_3 600	–	3.03±0.01	4.0	357
HCl 600	–	3.04±0.01	8.3	172
HBr 600	–	3.00±0.01	15.6	92

Table 3 – Initial (20 min) pseudo-first order kinetic constants, and relative correlation coefficients for the tested samples, in case of NO_x degradation in gas-solid phase, using both the solar and white lamp.

	Solar lamp		White lamp	
Sample	$k_{20}\times10^2$ (min^{-1})	R^2	$k_{20}\times10^2$ (min^{-1})	R^2
P25	4.427±0.194	0.990	0.657±0.043	0.991
HNO_3 450	1.021±0.025	0.997	0.618±0.015	0.997
HCl 450	0.691±0.018	0.997	1.515±0.019	0.999
HBr 450	1.682±0.104	0.981	1.534±0.030	0.998
HNO_3 600	0.609±0.022	0.997	–	
HCl 600	0.711±0.027	0.997	–	
HBr 600	–		–	

Figures and Captions

Fig. 1 – Scheme of the aqueous acid-peptised nanosynthesis method used to make titania sols.

Fig. 2 – PCS number size distributions for the HNO_3, HCl and HBr peptised titania sols. Their mean diameters are 3.61, 2.20 and 4.55 nm, respectively.

Fig. 3 – XRD patterns of the samples: (a) thermally treated at 450 °C **and P25**; (b) thermally treated at 600 °C; **(c) thermally treated at 800 °C**. **A**, **R** and **B** are symbols, standing for anatase, rutile, and brookite, respectively.

Fig. 4 – HR-TEM micrographs of samples (a) HCl 450, and (b) HBr 450.

Fig. 5 – Raman spectra of the samples: (a) thermally treated at 450 °C, **and P25**; (b) thermally treated at 600 °C; **(c) thermally treated at 800 °C**. The vertical bars represent the Raman peak shifts of: anatase (red), rutile (black), and brookite (blue).

Fig. 6 – Diffuse reflectance spectra (DRS) of the samples: (a) thermally treated at 450 °C; (b) thermally treated at 600 °C – in the inset is reported the transformed Kubelka-Munk function $[F(R_\infty)h\nu]^{0.5}$ *versus* energy; $\boldsymbol{M_g}$ is a symbol, standing for mid-gap band. (c) Diffuse reflectance spectrum of samples with HCl as counter-ion, and thermally treated at 450 °C, and, in the bottom, the plot of diffuse reflectance first derivative *versus* wavelength λ. The red curve is the result of the fitting, while the dashed vertical line represents the optical band gap, assigned to rutile in that sample.

Fig. 7 – FT-IR spectra of the samples thermally treated at 450 °C.

Fig. 8 – NO_x conversion rate results of the samples thermally treated at 450 °C: (a) with the solar lamp; (b) with the white lamp.

Fig. 9 – Photocatalytic activity results in liquid-solid phase, using UVA-light irradiation of: a) samples thermally treated at 450 °C; b) samples thermally treated at 600 °C. Photocatalytic activity

results in liquid-solid phase, using visible-light irradiation of: c) samples thermally treated at 450 °C; d) samples thermally treated at 600 °C.

Fig. 1

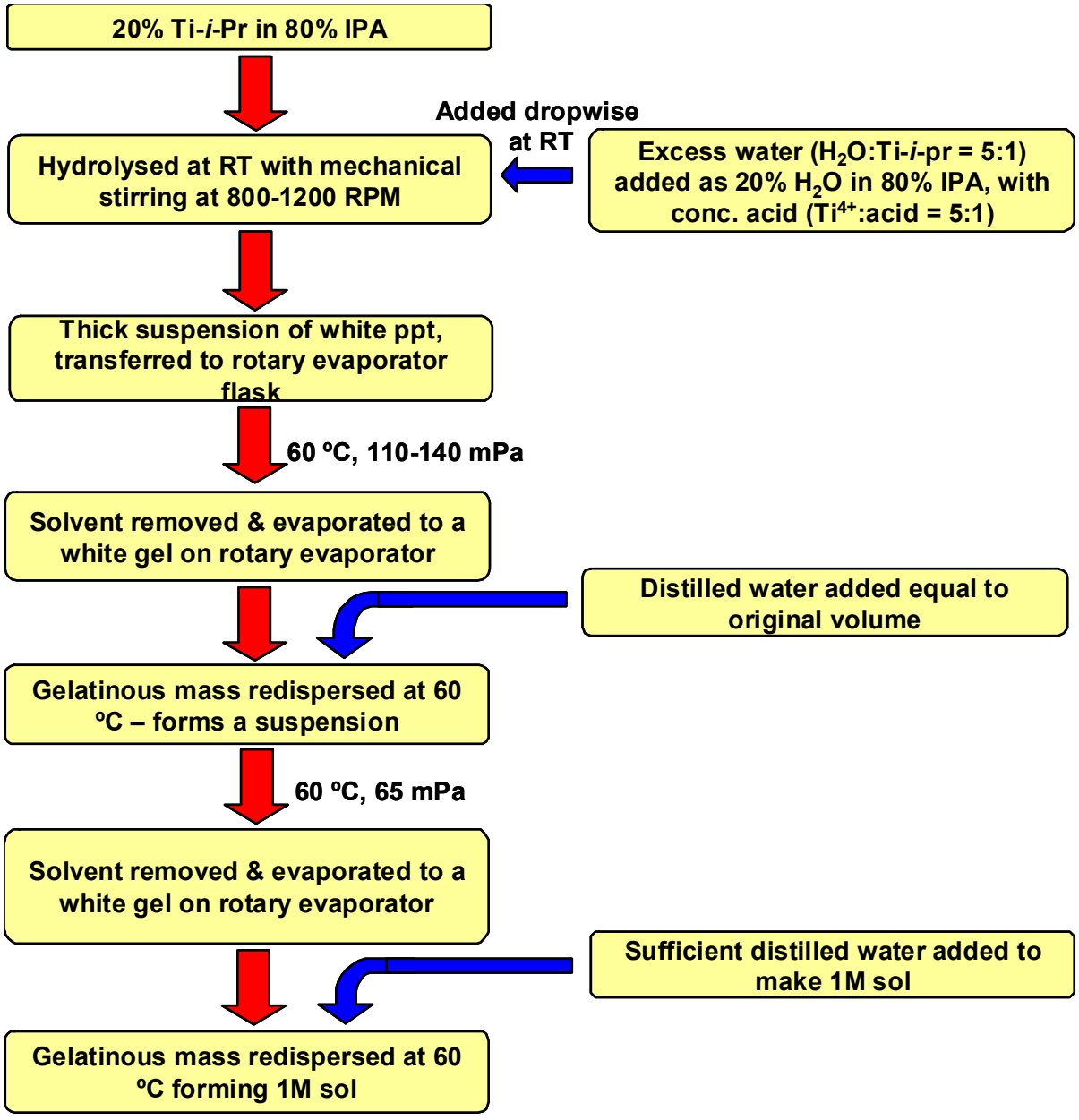

Fig. 2

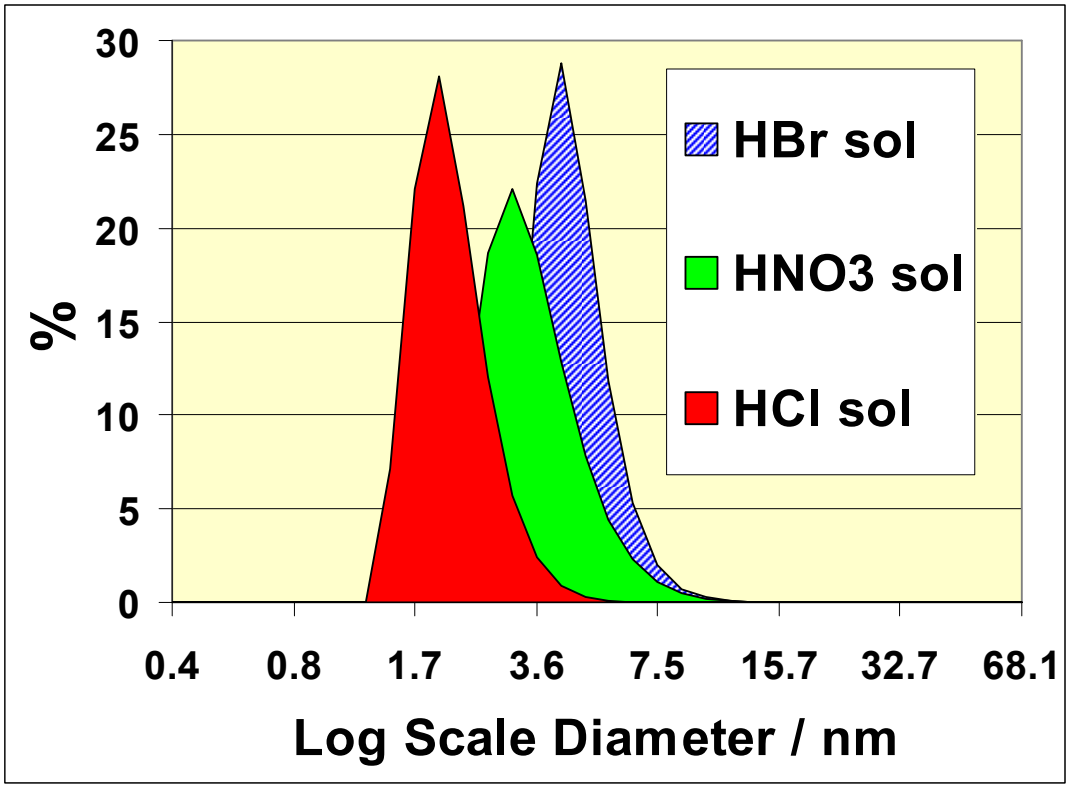

Fig. 3a

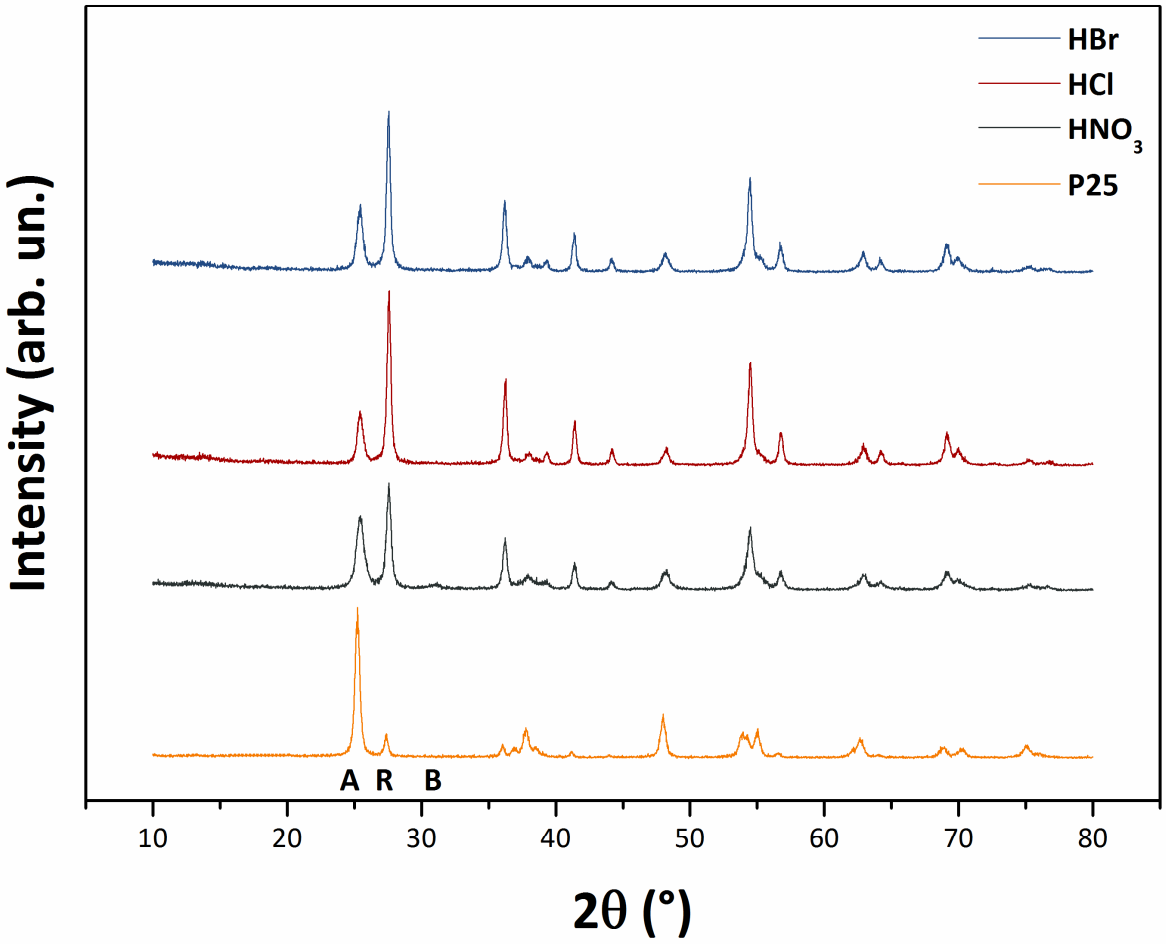

Fig. 3b

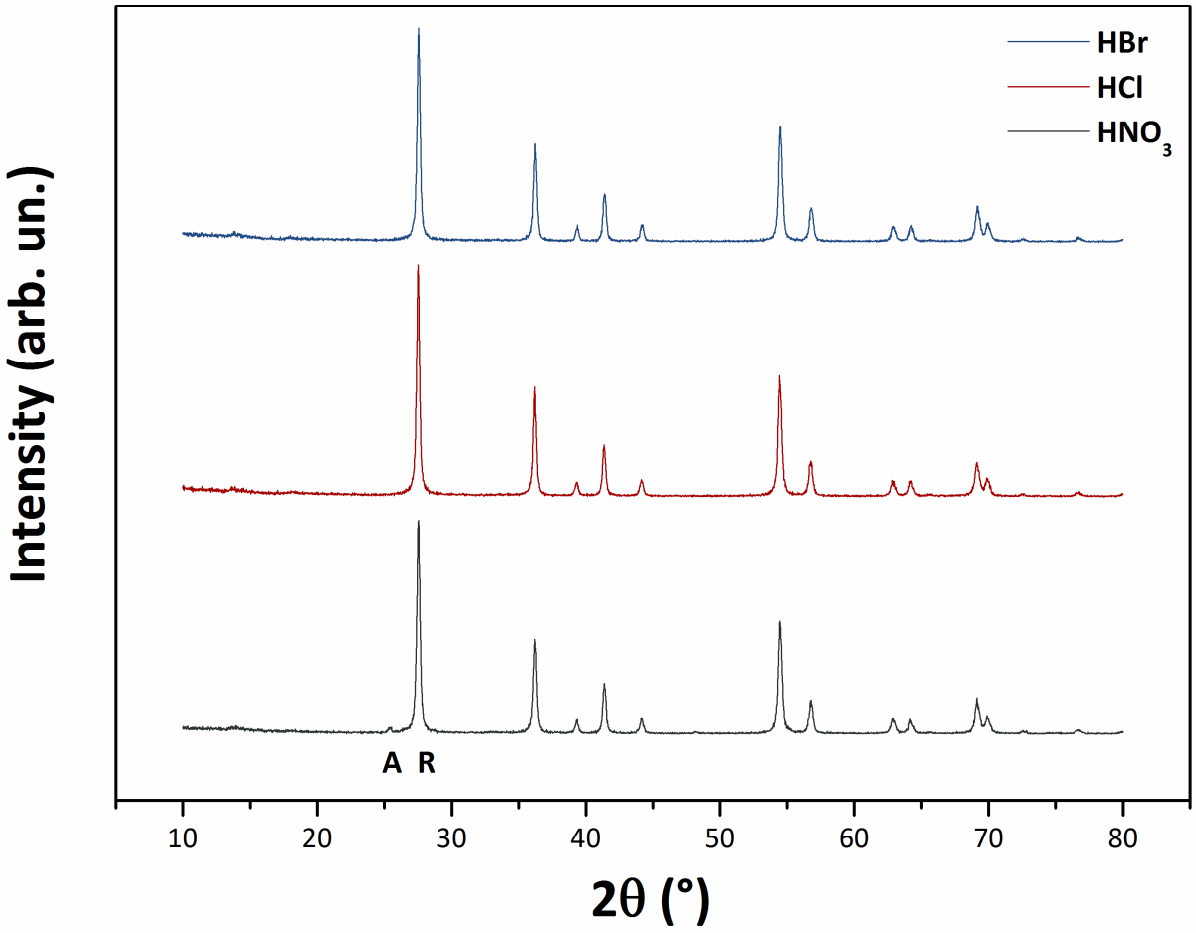

Fig. 3c

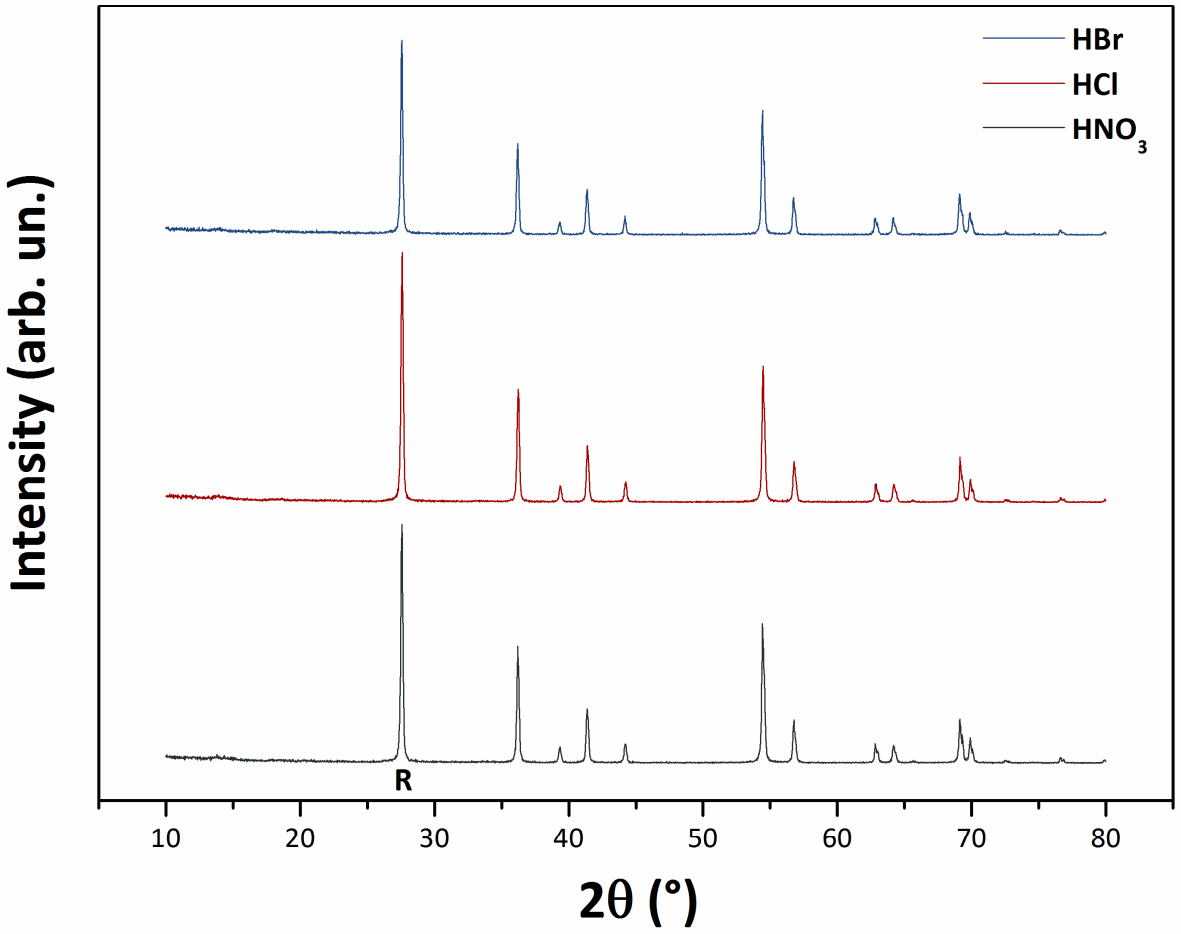

Fig. 4a

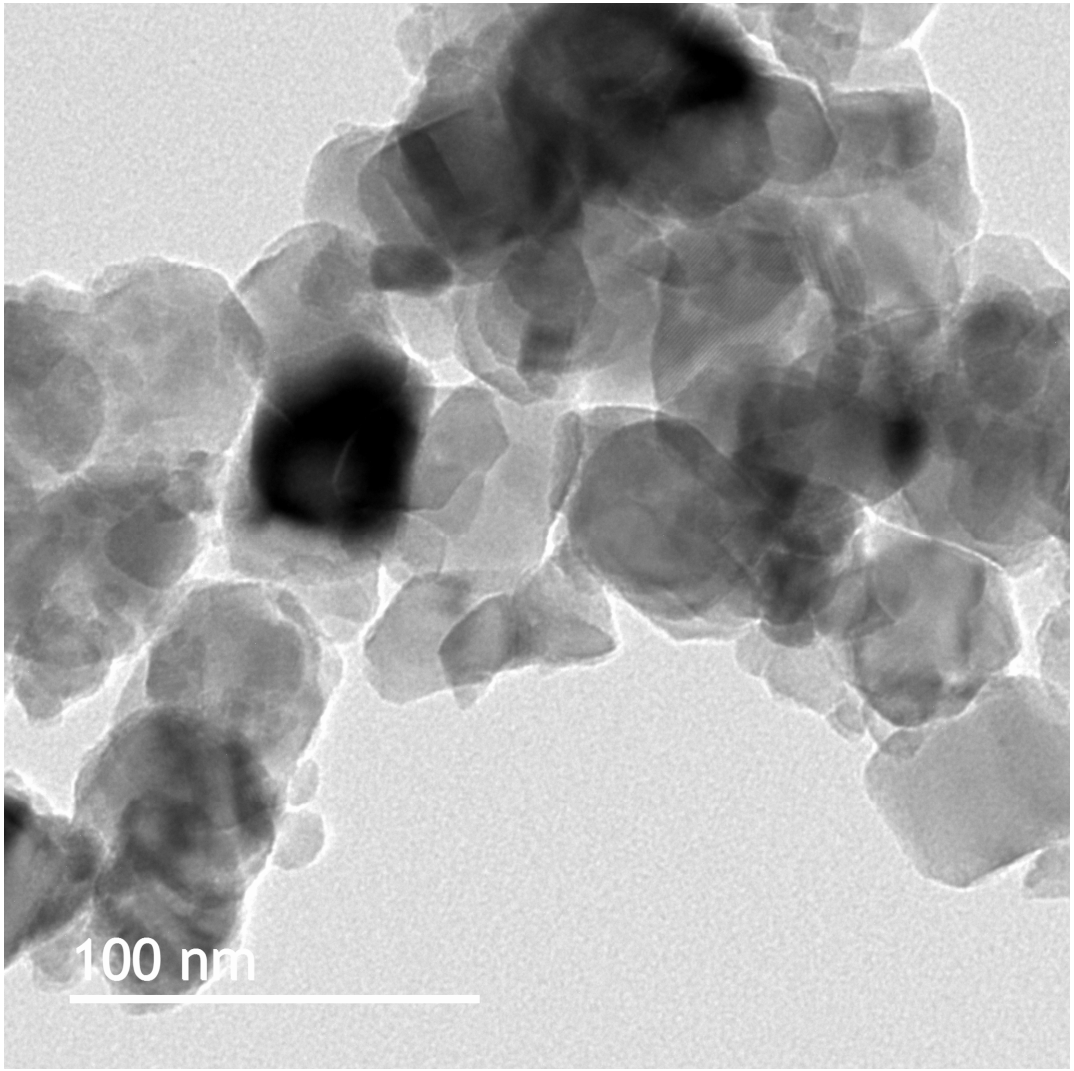

Fig. 4b

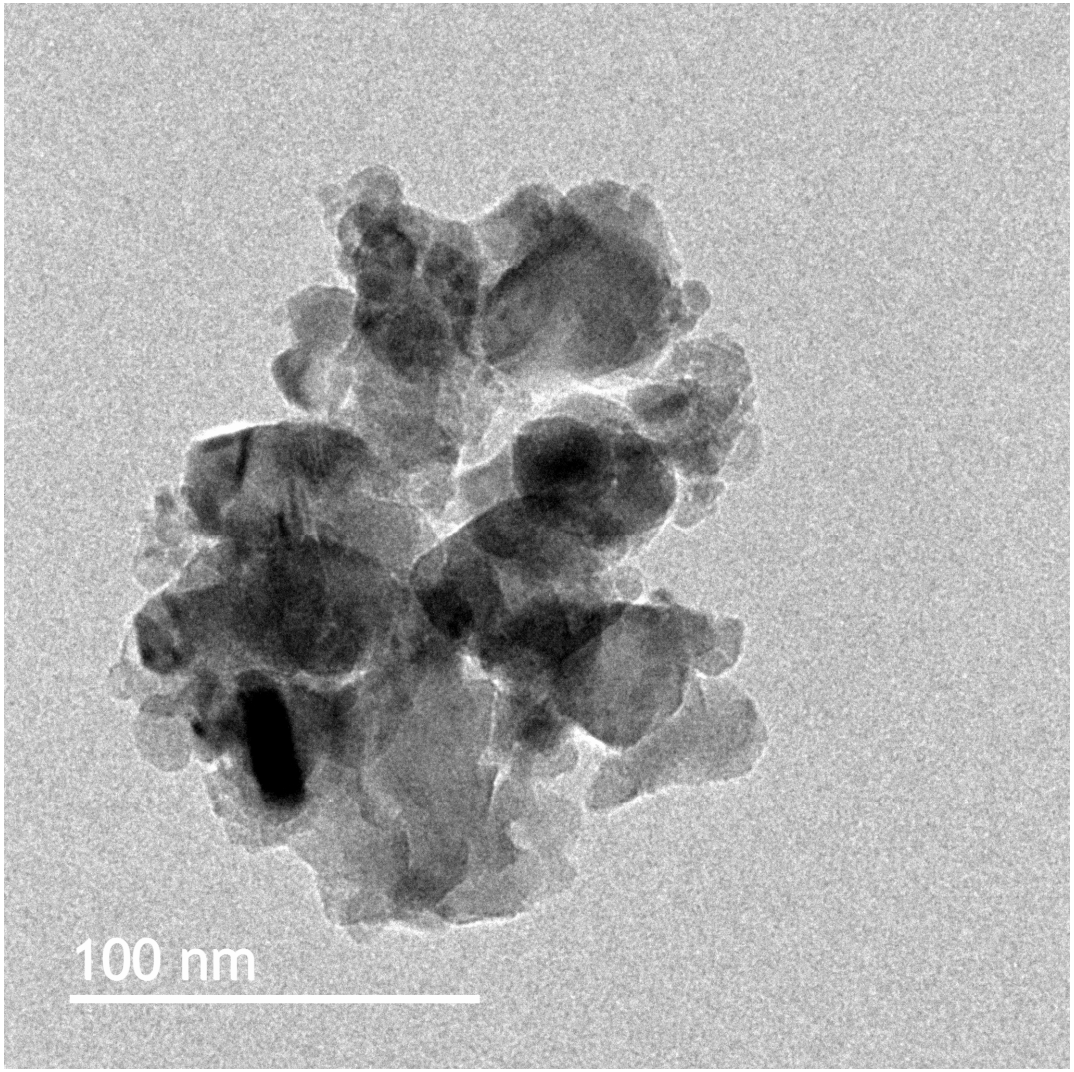

Fig. 5a

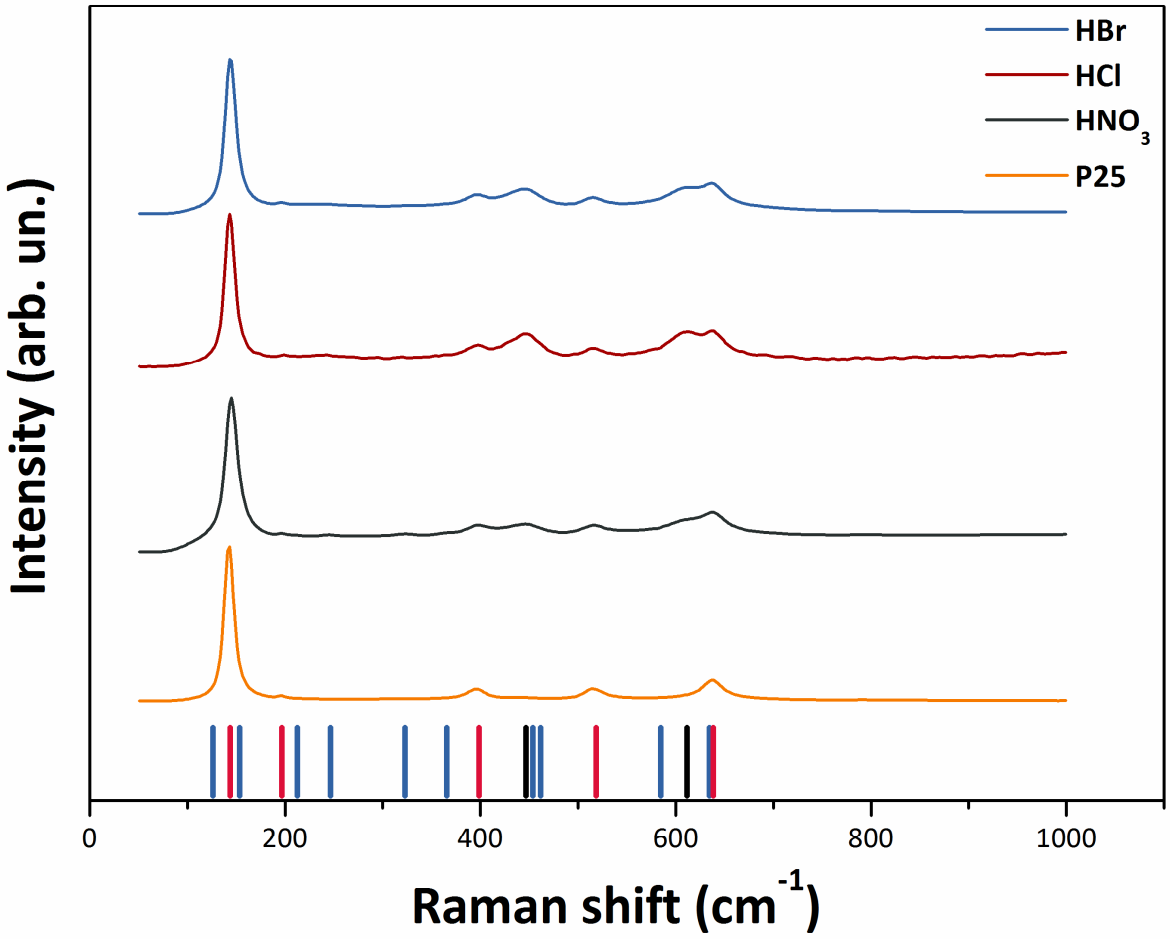

Fig. 5b

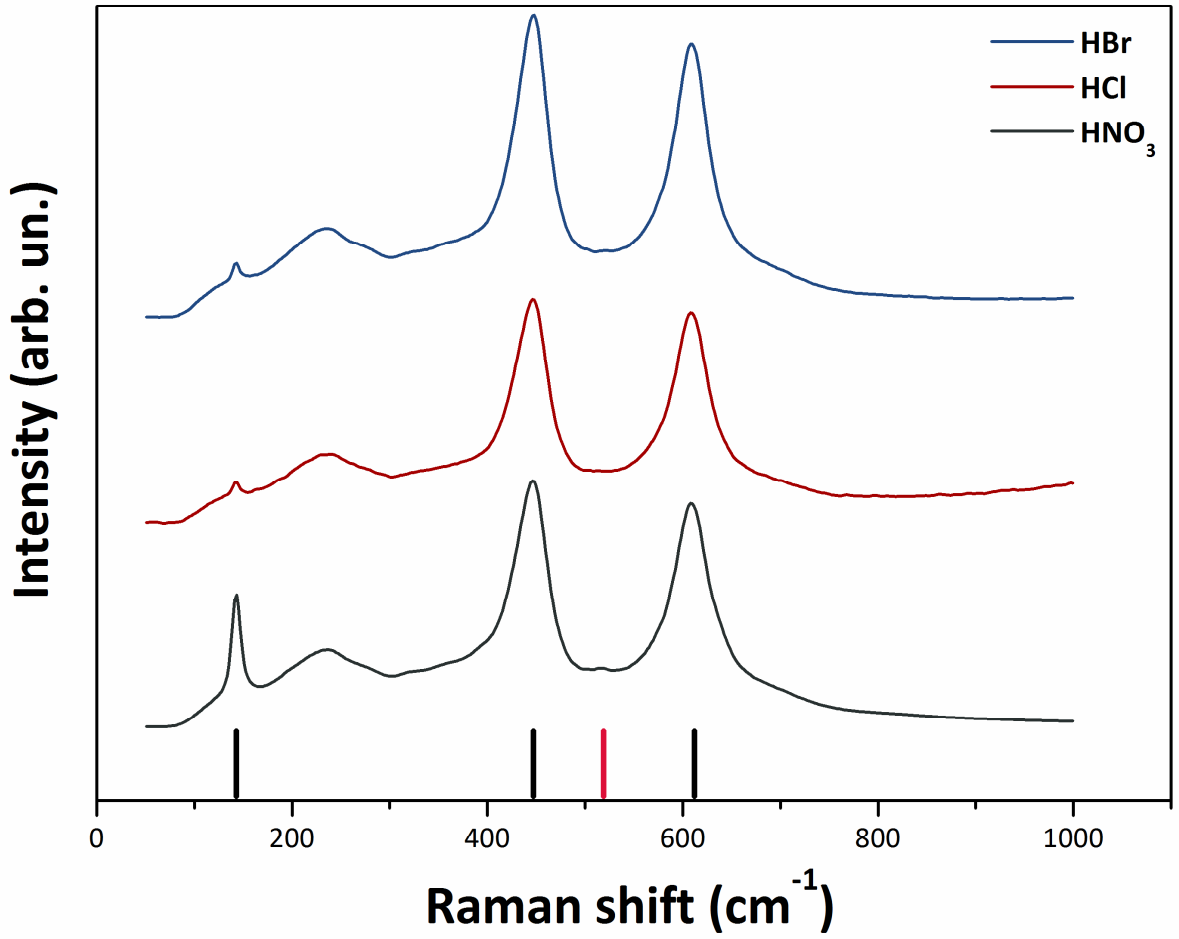

Fig. 5c

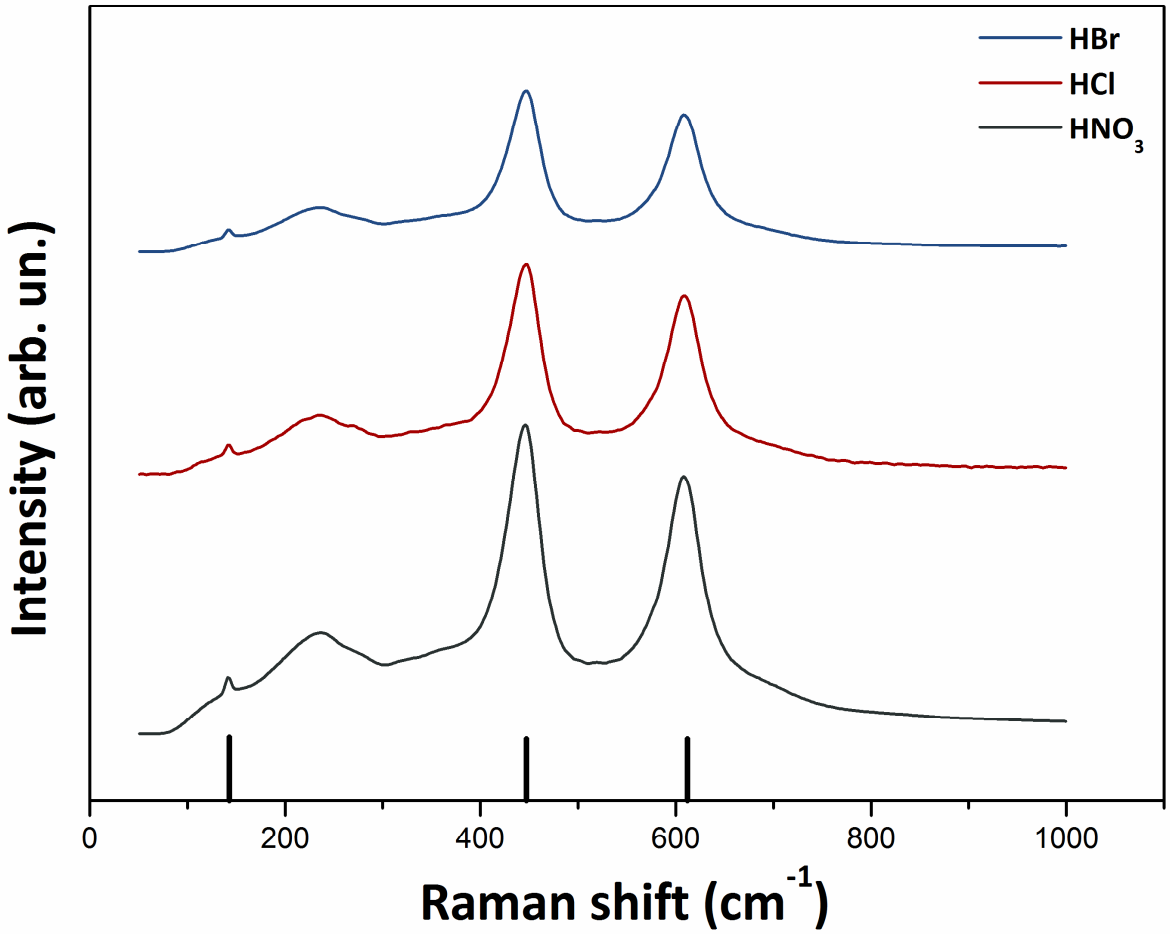

Fig. 6a

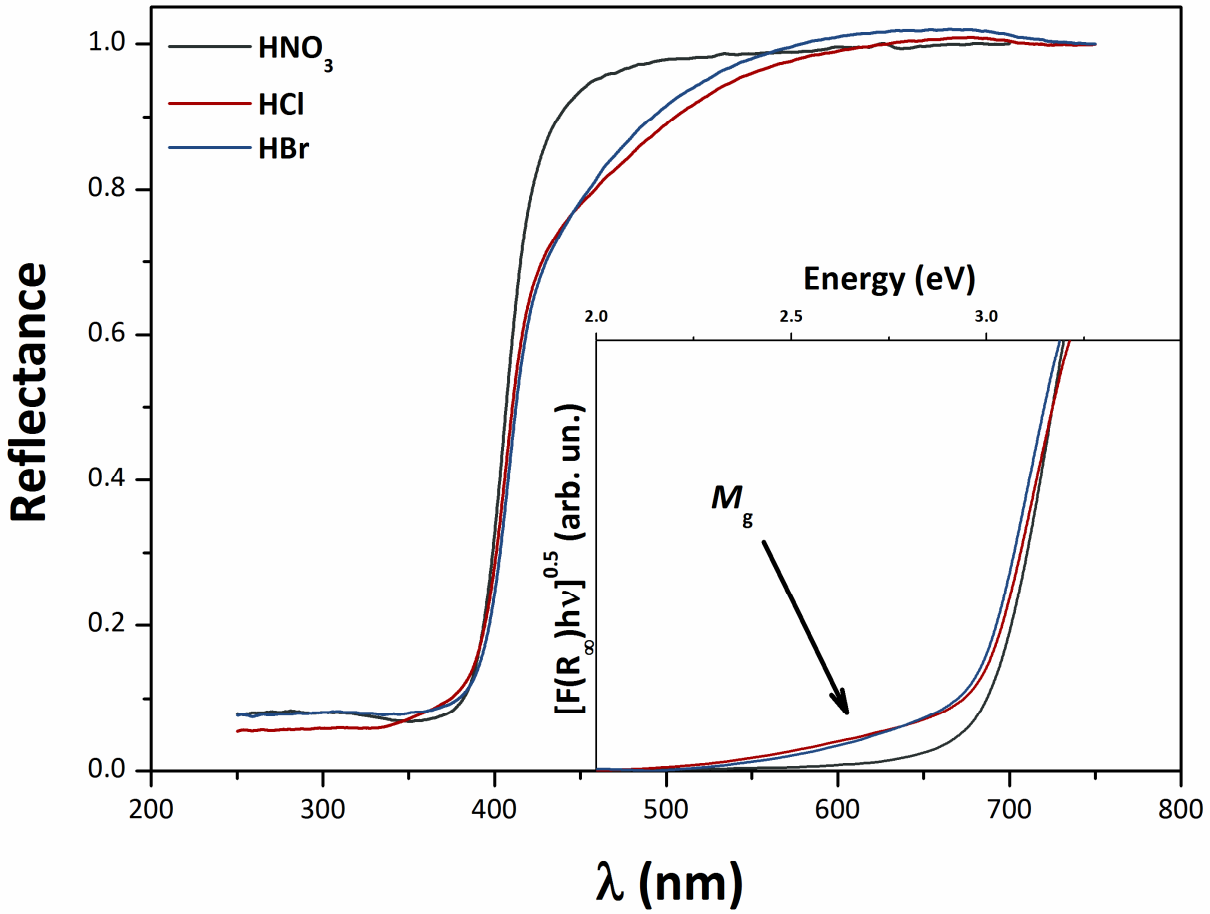

Fig. 6b

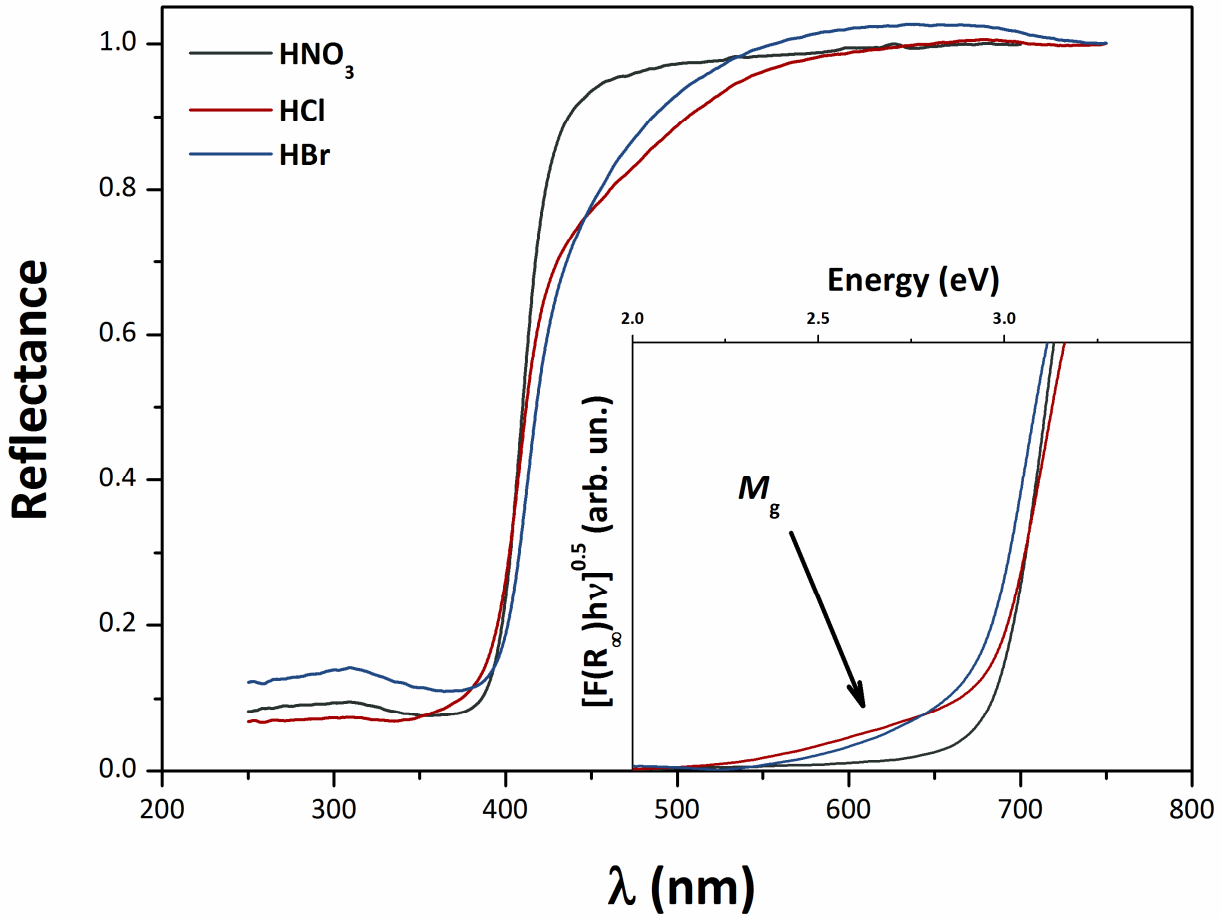

Fig. 6c

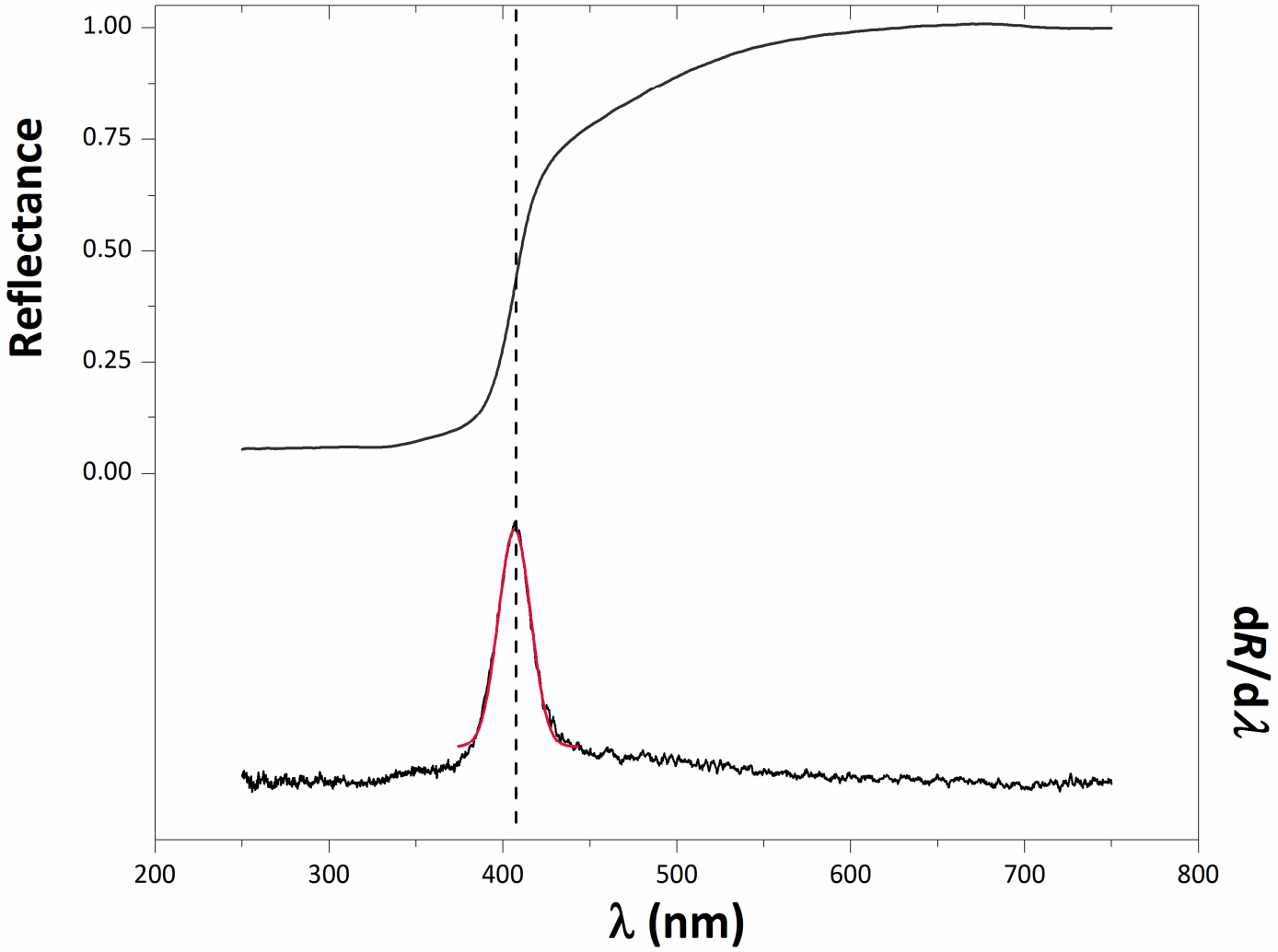

Fig. 7

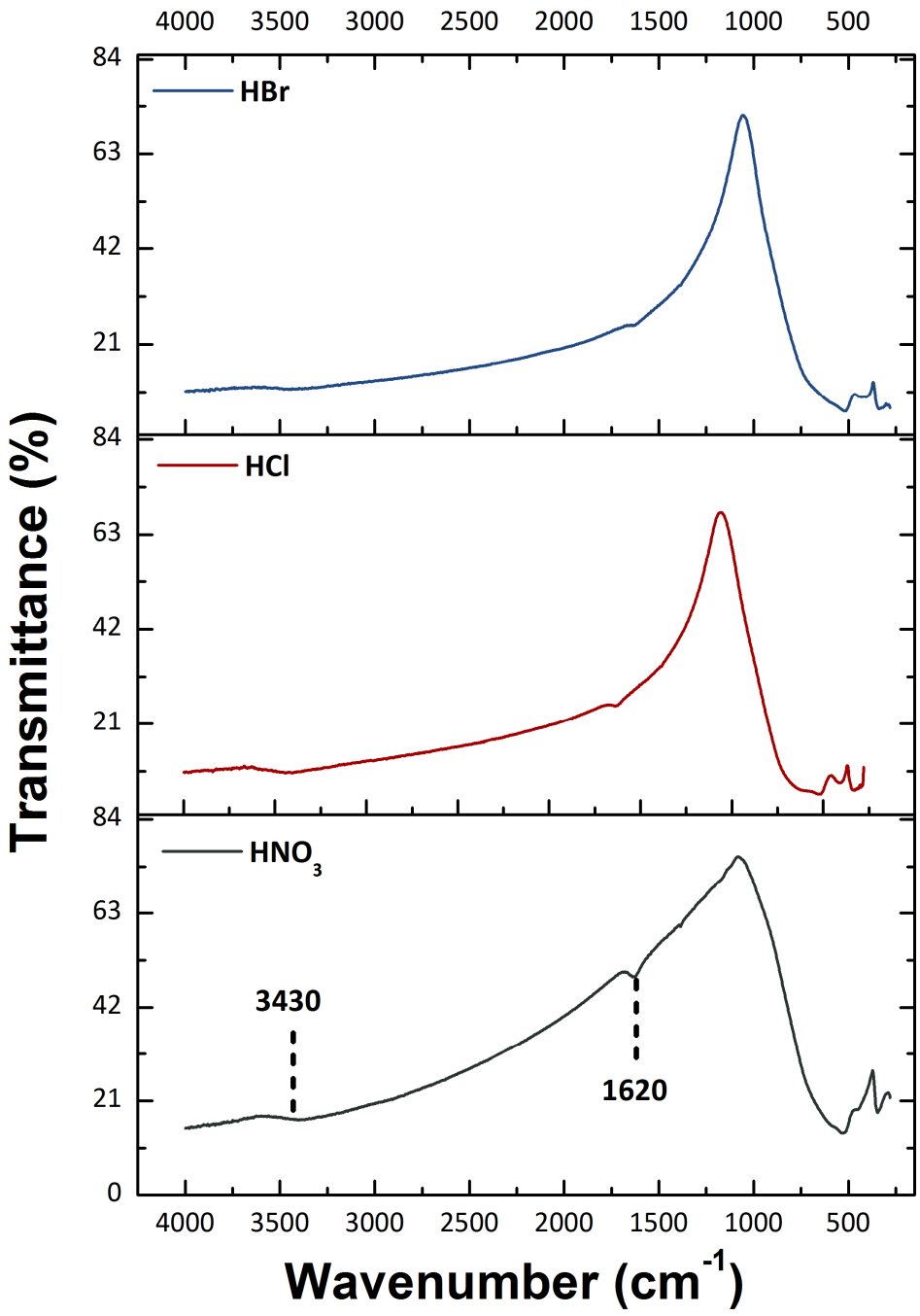

Fig. 8a

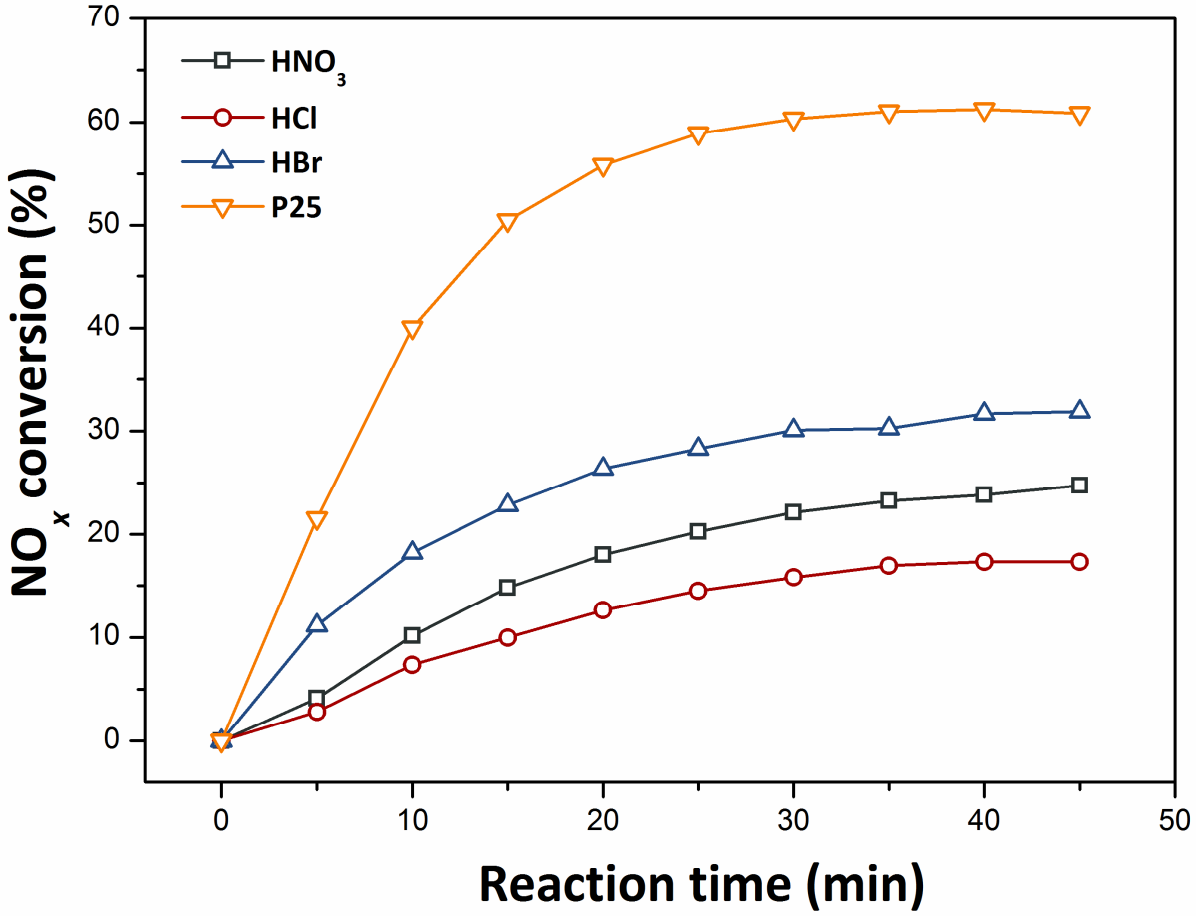

Fig. 8b

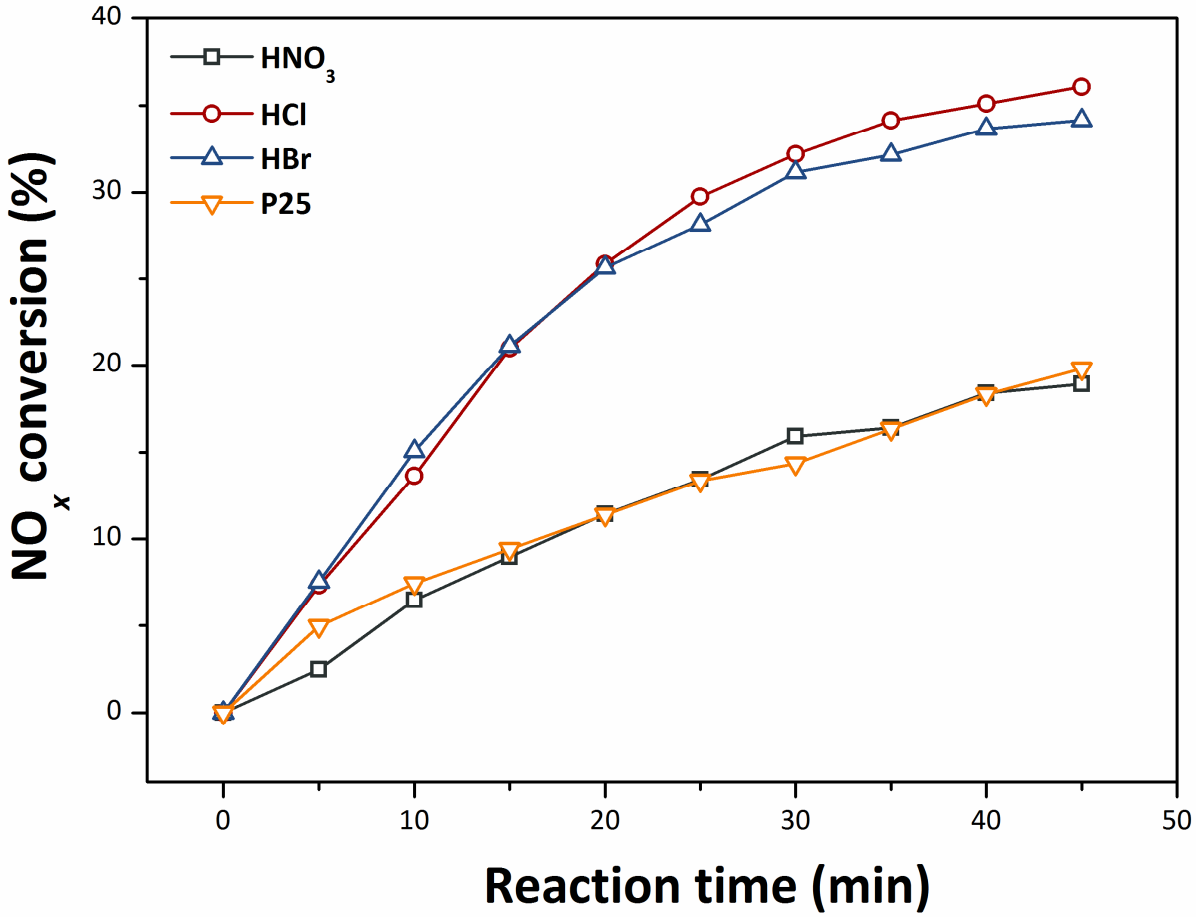

Fig. 9a

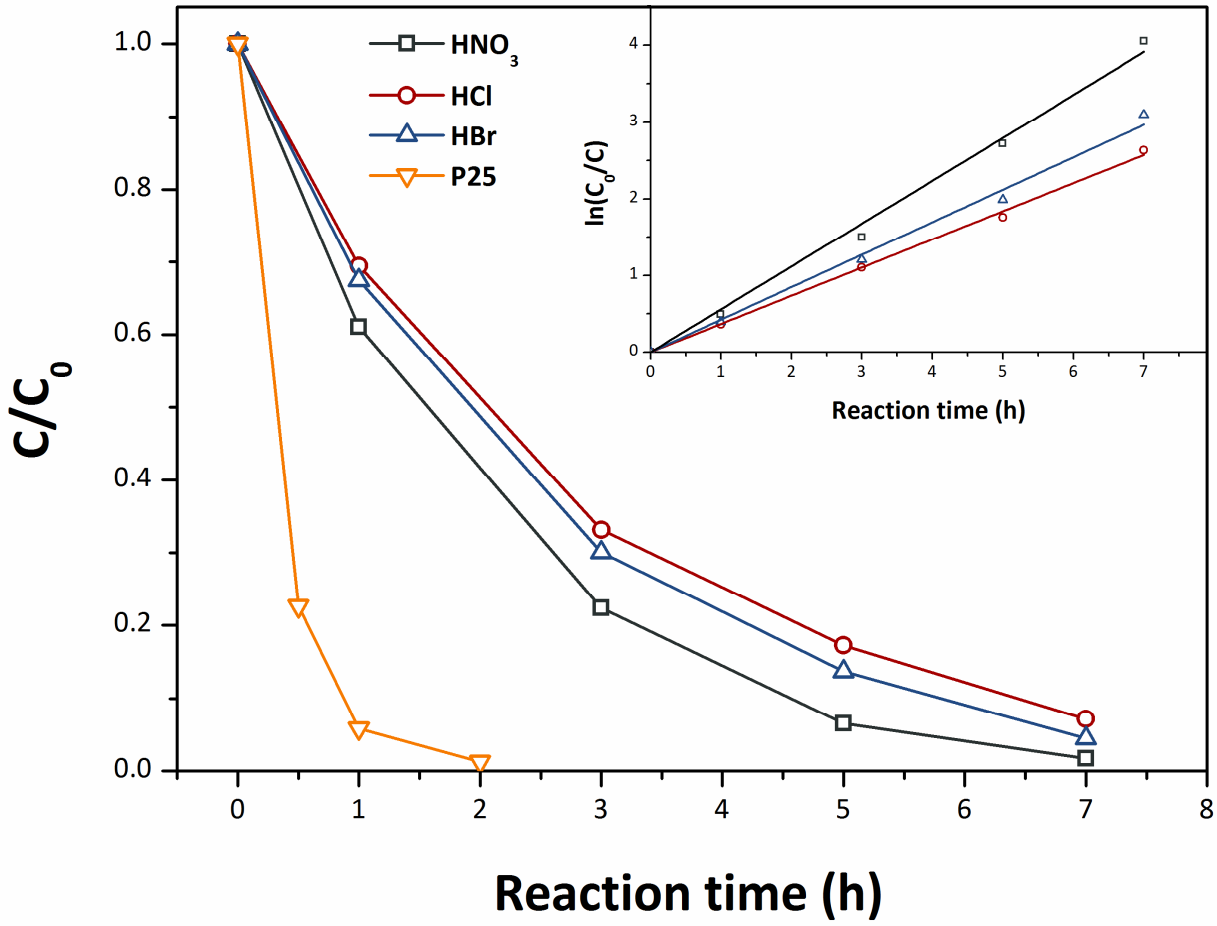

Fig. 9b

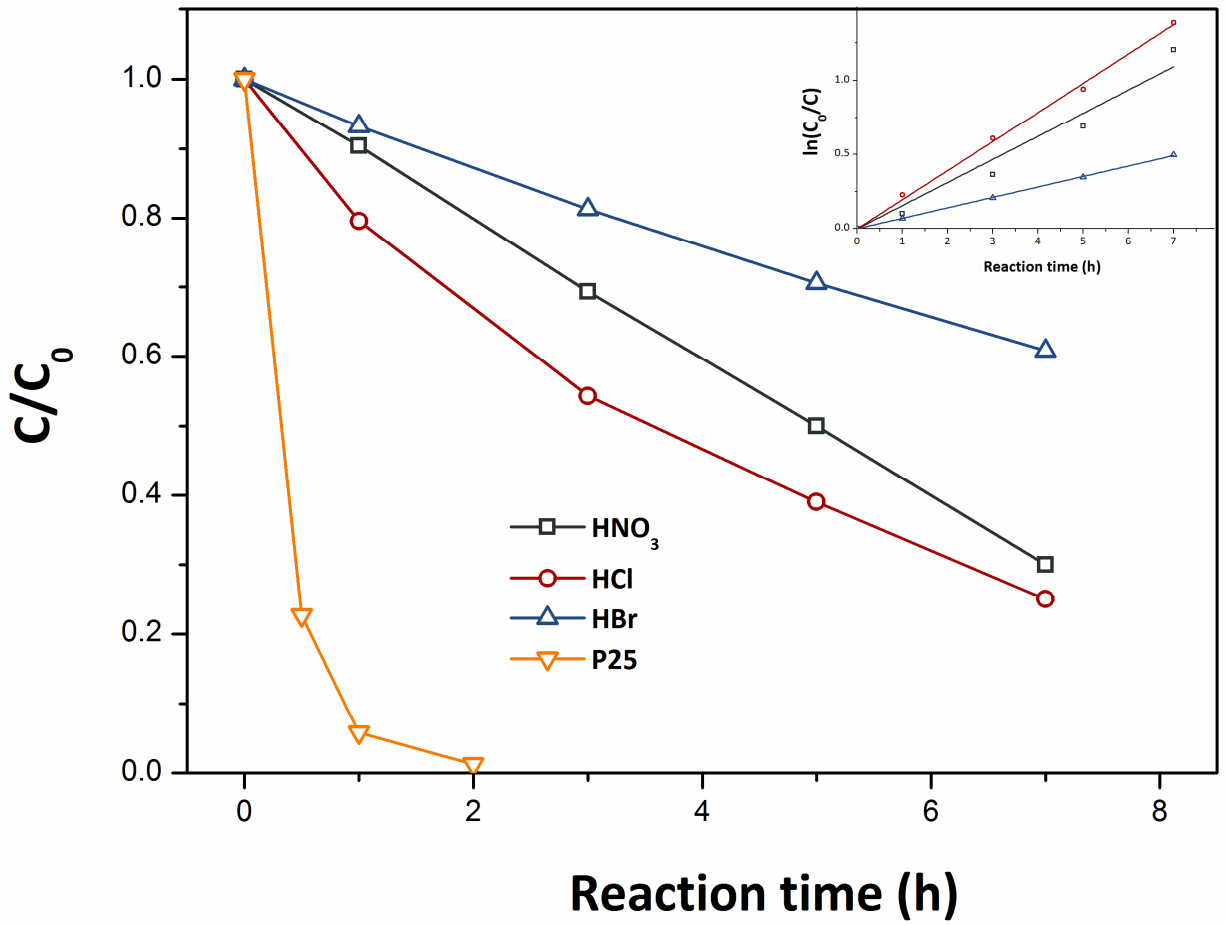

Fig. 9c

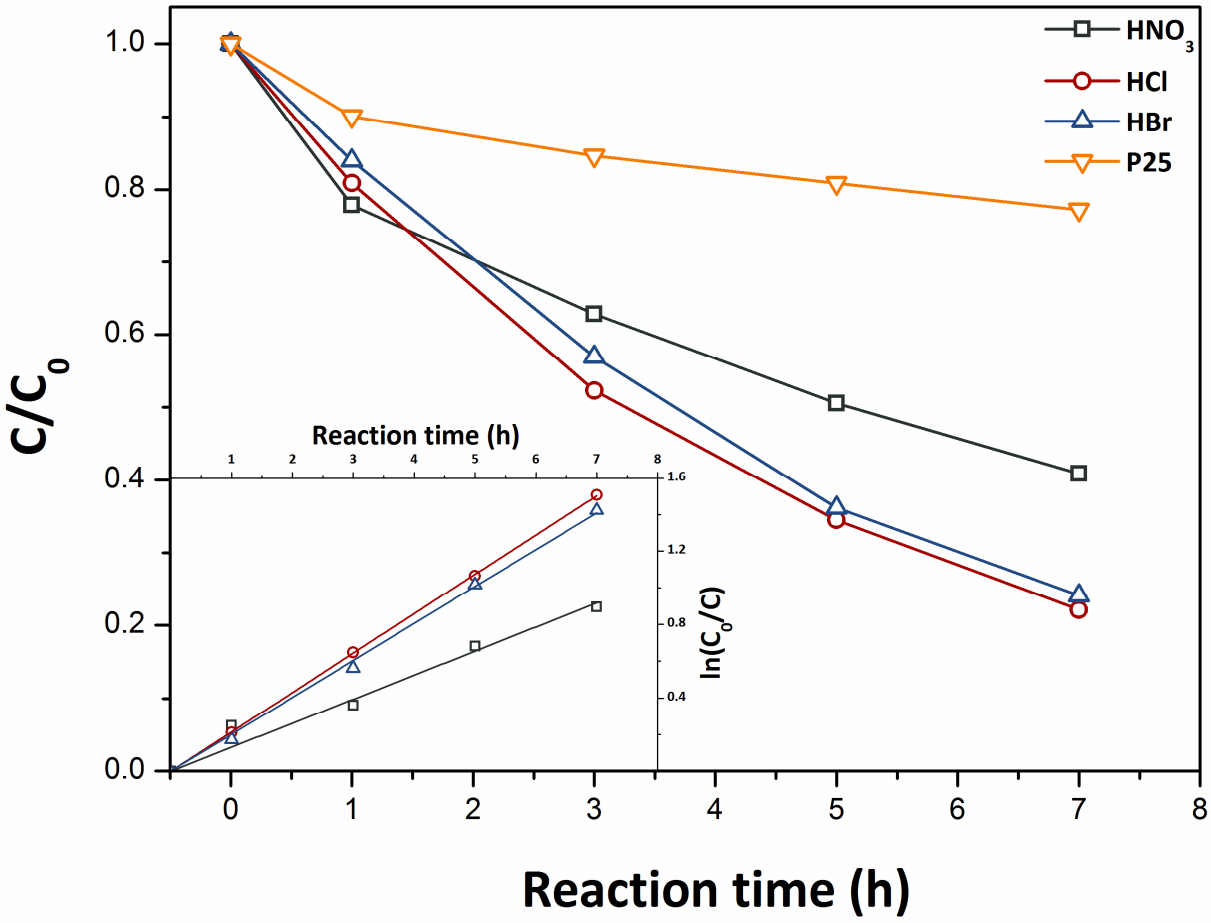

Fig. 9d